

INVESTIGATION OF PHYSICAL PROPERTIES OF A QUASI-1D QUANTUM MAGNET



A thesis submitted towards partial fulfilment of
BS-MS Dual Degree Programme

by

AMARTYA SINGH

under the guidance of

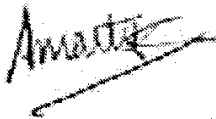
DR. CHRISTIAN HESS (IFW, DRESDEN)

INDIAN INSTITUTE OF SCIENCE EDUCATION AND RESEARCH
PUNE

Certificate

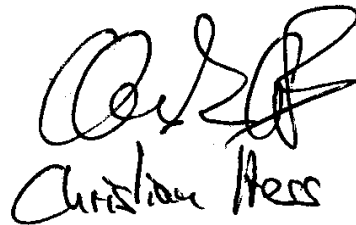
This is to certify that this thesis entitled "*Investigation of Physical Properties of a Quasi-1D Quantum Magnet*" submitted towards the partial fulfillment of the BS-MS dual degree programme at the Indian Institute of Science Education and Research Pune represents original research carried out by AMARTYA SINGH at IISER Pune and IFW Dresden (Germany), under the supervision of Dr. SURJEET SINGH (IISER Pune) and Dr. CHRISTIAN HESS (IFW Dresden) during the academic year 2012-2013.

Student



NAME

AMARTYA SINGH



Supervisor

NAME

Contents

I	Some Background Material	7
1	Introduction	8
1.1	Magnetic Dimer	8
1.1.1	Classical Dimer	9
1.1.2	Quantum Mechanical Dimer	9
1.2	1D Chain with $S=1/2$	11
1.2.1	Classical Case	12
1.2.2	Quantum Mechanical Case	12
1.3	The $S = 1/2$ Heisenberg Chain	13
1.3.1	Ferromagnetic Phase	13
1.3.2	Neél Phase	14
1.3.3	The Isotropic Heisenberg Chain	15
1.3.4	Magnetic Order and Quantum Fluctuations	16
1.3.4.1	Spin Wave Theory	18
1.3.5	Geometrical Frustration	18
1.4	Thermal Transport	19
1.4.1	Phonons	19
1.4.1.1	Thermal Conductivity due to Phonons	20
1.4.2	Transport due to Spin Excitations	22
1.4.2.1	Spinon-Defect Scattering	25
1.4.2.2	Spinon-Phonon Coupling	25
1.5	The Quasi-1D Spin Chain Compound SrCuO_2	26
1.5.1	Structure	26
II	Synthesis of the Crystals	30
2	Crystal Growth	31
2.1	Principles of single crystal growth	31
2.1.1	Travelling Solvent Floating Zone Technique	32
2.1.1.1	Stabilization Process	33
2.1.2	Phase Diagram of SrO-CuO Binary System	35
2.2	Experimental Realization of the TSFZ-Method	36
2.2.1	Furnace for Crystal Growth	36

2.2.2	Feed Rod	36
2.2.3	Choice of Solvent	37
2.2.4	Growth of Co and Zn doped SrCuO ₂	38
III	Experimental Techniques	40
3	Magnetic Susceptibility and Thermal Transport	41
3.1	Magnetic Susceptibility	41
3.2	Thermal Transport Measurement	41
3.2.1	Principles of Measurement of Heat Transport	41
3.2.2	Experimental Setup	43
3.2.3	Sources of Error	43
IV	Results and Discussions	47
4	Magnetic Susceptibility and Transport Properties	48
4.1	Magnetic Susceptibility	48
4.1.1	Effect of Magnetic Impurity	49
4.2	Thermal Transport	54
4.2.1	Effect of Magnetic Impurity (Co)	54
4.2.1.1	Co = 0.25%	54
4.2.1.2	Co = 1%	60
V	Summary	67
5	Attempt towards a coherent picture	68

Abstract

The aim of the present study is to investigate the low temperature bulk magnetic properties and transport properties of a low dimensional quantum magnet SrCuO_2 . Along with another member from the cuprate family Sr_2CuO_3 , this compound offers an excellent realization of 1D spin chains in a bulk crystal. However, unlike Sr_2CuO_3 which has well separated linear chains of Cu-O-Cu, the basic structural units of the spin chains in SrCuO_2 comprises of two linear chains of Cu-O-Cu coupled together to form a ribbon. The nearest neighbour (with a localized spin) of each Cu ion in such an arrangement is another Cu ion in the neighbouring chain of the ribbon. Thus, the Cu-Cu chain is a zig-zag chain which explains why this compound is also popularly known as a zig-zag chain compound. This unique structure leads to an inherent frustration in the system due to the fact that the next nearest neighbour Cu spins along the linear Cu-O-Cu chain couple antiferromagnetically, while the nearest neighbour Cu spins couple ferromagnetically. This inherent frustration is understood to play a key role at determining the behaviour of the system at very low temperatures.

Previous studies on the magnetic ground state of this compound have revealed that there is no long range order (LRO) down to temperatures as low as 2K. Frustration is believed to play a key role in suppressing the LRO in the system. In order to better understand the role played by frustration we have successfully grown single crystals of SrCuO_2 , which are lightly doped with varying concentrations (0.25%, 0.5% and 1%) of non-magnetic (Zn) and magnetic (Co) impurities. The technique used to grow these crystals is the Traveling Solvent Floating Zone (TSFZ) method using the four-mirror optical furnace at IISER (Pune).

DC Magnetization/Susceptibility measurements were performed by Koushik Karmakar (PhD Student, Physics, IISER Pune) at IISER, where it was found that the non-magnetic impurities (Zn^{2+}) break the chains into segments, where at the free ends of these segments effective paramagnetic moments are induced. However, no LRO is observed down to 2K. For magnetic impurities (Co^{2+}) the behaviour is more complex. The susceptibility shows a highly anisotropic behaviour which is also temperature dependent. There is no transition peak observed in susceptibility measured along the crystallographic a and b directions, whereas a prominent peak in the susceptibility at around 5K is measured along the c direction, which indicates a highly anisotropic ordering behaviour. The transition temperature scales with the concentration of the Co^{2+} ions which

can be taken as an evidence to assert that the Co ions are present in the spin chains. Below the transition peak, ZFC and FC measurements reveal a splitting/hysteresis which points towards a spin glass/freezing behaviour.

Thermal transport studies were performed on two concentrations of Co doped samples at the IFW Dresden under the supervision of Dr. Christian Hess to gain an improved understanding of the effect of doping of magnetic impurities on the elementary excitations (spinons) in the spin chains and their coupling with phonons.

In the near future it is planned to perform μSR and neutron scattering studies at the Paul Scherrer Institute (PSI), Switzerland in the temperature range below 5K to understand the local spin behaviour in the case of Co doped single crystals of $SrCuO_2$.

Acknowledgements

I would like to especially thank:

- Dr. Surjeet Singh (Assistant Professor, Physics, IISER Pune) for giving me the opportunity to work on this project and for his constant encouragement and support.
- Prof. Dr. B. Büchner (Director, Institute for Solid State Research (IFF), IFW, Dresden) for giving me the opportunity to perform the thermal transport measurements in the Transport and Tunnelling Group of Dr. C. Hess
- Dr. C. Hess (Group Leader, Transport and Tunnelling Group, IFF, IFW, Dresden) for giving me the opportunity to do the thermal transport studies and for his infinite patience, support and encouragement throughout the duration of my work at the IFW.
- Koushik Karmakar (PhD Student, IISER Pune) for his selfless help and guidance during the growth of the crystals and for the useful discussions on the physics of these systems.
- Ashwin Mohan (PhD Student, Transport and Tunnelling Group, IFF, IFW Dresden) for unconditional help which made it possible to perform the thermal transport measurements in a short span of time. The discussions on various physical aspects of these systems were particularly illuminating and insightful.
- Oleg Mityashkin (PhD Student, Transport and Tunnelling Group, IFF, IFW Dresden) for taking out time to guide me with my measurements and providing valuable inputs.

I must also acknowledge the help and encouragement received from the other group members (both at IISER Pune and IFW Dresden), friends, and last but not the least, my family who have been a pillar of strength through every single moment of my existence.

Part I

Some Background Material

Chapter 1

Introduction

The simplest system with a permanent magnetic moment in its ground state is the hydrogen atom.¹ The magnetic moment arises due to the intrinsic degree of freedom of the electron called *spin*. The magnitude of this moment is given by,

$$\mu = g\mu_B S \quad (1.1)$$

where g is the Landé factor and S is the magnitude of the component of spin along a given axis. As it turns out according to Dirac's Relativistic Theory, $g \approx 2$, and we know that the magnitude of S for a single electron which is a fermion, is $S = 1/2$. Therefore the effective magnetic moment of this system is,

$$\mu = \mu_B \quad (1.2)$$

where $\mu_B = \frac{e\hbar}{2mc} = 0.927 \times 10^{-20} \text{ emu}$ (in CGS-Gauss units) is called the *Bohr Magneton*. It provides a natural realization of a unit in which the magnetic moments of other systems can be expressed and compared.

However, an isolated magnetic moment in space offers very little information when it comes to explaining the behaviour of a multitude of magnetic systems found in nature. In order to understand the physics of magnetic systems we have to understand the nature of the interactions between the magnetic moments. The simplest system which helps us take the first step towards such an understanding is a *dimer*.

1.1 Magnetic Dimer

As the name suggests a Magnetic Dimer consists of two interacting magnetic moments or *spins* (henceforth in this text, only the term spin will be used without any loss of information). Is it possible to write down an expression

¹Remarkably, the magnetic moment of an isolated electron measured in a frame of reference in which it is at rest is the same as the magnetic moment of the hydrogen atom in its ground state.

which accounts for the interaction of these two spins? As it turns out, it is possible to write down a simple expression for the interaction as,

$$\mathcal{H} = J(\mathbf{S}_1 \cdot \mathbf{S}_2) \quad (1.3)$$

Here J determines the strength of the coupling between the two spins, while \mathbf{S}_i denotes a three dimensional vector in the classical case or a three dimensional spin operator expressed in terms of the three Pauli matrices for the quantum mechanical case. This model was first suggested by Heisenberg in 1928 [3], wherein he also gave the correct microscopic explanation for the exchange interaction J . He showed that exchange interaction is not a fundamental force in itself but is a quantum mechanical effect with the fundamental force responsible being the Coulomb force. We will discuss both the classical case and the quantum mechanical case for this model, in turn now.

1.1.1 Classical Dimer

Assuming that the spin vectors behave like classical three dimensional vectors, we can write down the energy term as,

$$\mathcal{H}_{Classical} = J(S_1 S_2 \cos \theta) \quad (1.4)$$

We want to arrive at the ground state of such a system. Depending on the sign of J we will have two cases:

- +ve J (Antiferromagnetic): The system has lowest energy when the spins are aligned antiparallel to each other ($\theta = 180^\circ$).
- -ve J (Ferromagnetic): The system has lowest energy when the spins align parallel to each other ($\theta = 0^\circ$).

The energy of the ground state for both the cases is,

$$E_0 = -|J|S^2 \quad (1.5)$$

Note that the ground state energy of the system is rotationally invariant since it is solely dependent on the relative orientation of the two spins (parallel or antiparallel). The energy of the excited system can itself vary continuously from the ground state energy to the highest energy (since $\cos\theta$ varies continuously between -1 to $+1$),

$$E_{Highest} = |J|S^2 \quad (1.6)$$

1.1.2 Quantum Mechanical Dimer

In the quantum mechanical case the spin terms are replaced by spin operators which are expressed in terms of the Pauli Matrices as,

$$S_i^x = \frac{\hbar}{2} \sigma_i^x \quad (1.7)$$

$$S_i^y = \frac{\hbar}{2} \sigma_i^y \quad (1.8)$$

$$S_i^z = \frac{\hbar}{2} \sigma_i^z \quad (1.9)$$

We need to find a complete set of eigenstates for this system. This can be done by first identifying a complete orthonormal set of states for the system. After expressing \mathcal{H} in this basis, we can subsequently diagonalize to find the eigenstates for this system. A convenient basis for the dimer can be written down in Dirac notation as,

$$|++\rangle, |+-\rangle, |-+\rangle, |--\rangle \quad (1.10)$$

where the first sign (+ or -) corresponds to the spin state of the first spin (up or down), while the second sign corresponds to the spin state of the second spin.

Writing down \mathcal{H} in terms of spin operators we get,

$$\mathcal{H} = J(\mathbf{S}_1 \cdot \mathbf{S}_2)$$

$$\mathcal{H} = J(S_1^x S_2^x + S_1^y S_2^y + S_1^z S_2^z) \quad (1.11)$$

We can re-express \mathcal{H} in terms of raising and lowering operators which are defined as,

$$S_j^+ = S_j^x + iS_j^y$$

$$S_j^- = S_j^x - iS_j^y$$

to write,

$$\mathcal{H} = J[S_1^z S_2^z + \frac{1}{2}(S_1^+ S_2^- + S_1^- S_2^+)] \quad (1.12)$$

Now we can evaluate the elements of the matrix of \mathcal{H} expressed in terms of the basis states listed out in (1.10). While evaluating the matrix elements we must keep in mind the following point:

- The operators which act on different spins commute with each other.

This means that the order in which these operators act on the state vectors of the basis set is immaterial since the operator which acts on spin 1 does not affect the other spin and vice versa. The matrix of \mathcal{H} obtained for the basis set of (1.10) is,

$$\mathcal{H} = J \begin{bmatrix} \frac{1}{4} & 0 & 0 & 0 \\ 0 & -\frac{1}{4} & \frac{1}{2} & 0 \\ 0 & \frac{1}{2} & -\frac{1}{4} & 0 \\ 0 & 0 & 0 & \frac{1}{4} \end{bmatrix} \quad (1.13)$$

The eigenvalues of the characteristic equation of this matrix are,

$$E = \frac{J}{4}, \frac{J}{4}, \frac{J}{4} - \frac{3J}{4} \quad (1.14)$$

The eigenstates corresponding to the eigenvalue $\frac{J}{4}$ are,

$$\psi_1 = \begin{bmatrix} 1 \\ 0 \\ 0 \\ 0 \end{bmatrix}, \psi_2 = \begin{bmatrix} 0 \\ \frac{1}{\sqrt{2}} \\ \frac{1}{\sqrt{2}} \\ 0 \end{bmatrix}, \psi_3 = \begin{bmatrix} 0 \\ 0 \\ 0 \\ 1 \end{bmatrix} \quad (1.15)$$

While for the eigenvalue $-\frac{3J}{4}$ the eigenstate is,

$$\psi_4 = \begin{bmatrix} 0 \\ \frac{1}{\sqrt{2}} \\ -\frac{1}{\sqrt{2}} \\ 0 \end{bmatrix} \quad (1.16)$$

Let us have a look at the most important results that we have obtained so far:

- First, in contrast to the classical case, states with only two discrete energy levels are allowed, i.e. the energy levels are quantized.
- Second, if we compare the energy of the ground state for the case of antiferromagnetic coupling between the two spins of the dimer, we see that the ground state energy for the quantum case ($-\frac{3J}{4}$) is significantly lesser than the energy of the ground state for the classical case ($-\frac{J}{4}$).

The second result brings to light the role an additional symmetry plays in determining the energy levels of the system. This symmetry is the intrinsic rotational symmetry of the spin space and is called the $SU(2)$ symmetry in Group Theory notation.

1.2 1D Chain with $S=1/2$

The case of the magnetic dimer has shown us a few pointers as to the role played by the quantum nature of the spins. Can we extend the same model of interaction between the spins to explain the behaviour of the next logical extension of spins, namely a 1D spin chain? Suppose we assume the same form of interaction between the nearest-neighbour (NN) spins, then we can write down the Hamiltonian for the system as,

$$\mathcal{H} = J \sum_{i=1}^N \mathbf{S}_i \cdot \mathbf{S}_j \quad (1.17)$$

Assuming periodic boundary conditions, we can write this down as,

$$\mathcal{H} = J \sum_{i=1}^N \mathbf{S}_i \cdot \mathbf{S}_{i+1} \quad (1.18)$$

where $i + N = i$.

1.2.1 Classical Case

As for the case of the magnetic dimer, we have two cases corresponding to the sign of J :

- -ve J (Ferromagnetic): The lowest energy of a pair of spins is attained when the two spins align in parallel to each other. For the entire system the pairwise interaction will yield the lowest energy when all the spins align along the same direction. The energy of this state is given by,

$$E = -N|J|S^2 \quad (1.19)$$

- +ve J (Antiferromagnetic): The lowest energy for every pair of spins in this case is attained for an even number of spins and is the same as the energy for the ferromagnetic case.

1.2.2 Quantum Mechanical Case

As was the case for the magnetic dimer, the ground state energy of 1D chain with ferromagnetic (-ve J) coupling between NN spins for the quantum mechanical case is the same as the classical ground state energy. We can calculate this energy as the solution of the eigenvalue problem with the eigenstate corresponding to the state with all the spins aligned along a given direction (say along z).

The case for antiferromagnetic (+ve J) coupling offers more insight into the role played by the quantum nature of spins in determining the ground state properties of the 1D chain. Obtaining the ground state for the antiferromagnetic case is a highly non-trivial problem since the state corresponding to the classical ground state configuration (with all NN pairs aligned antiparallel to each other) is no longer an eigenstate. Hans Bethé in 1931 was the first to give a form for the ground state wavefunction using his famous *ansatz*[4]. In the following the basic ideas used by Bethé to arrive at the *ansatz* equations are briefly sketched:

- As the first step, free particle wavefunctions for the elementary excitation (single spin inversion) in a ferromagnetic chain are assumed.
- The case for two inverted spins leads to additional constraints on the quasi-momentum of the free particle solutions resulting from the consideration of the case when the two inverted spins sit on neighbouring sites.
- Gradually the number of inverted spins may be increased while respecting the additional constraints obtained for the case of two inverted spins.

- The antiferromagnetic ground state consists of the case when exactly half the spins of the chain are inverted.

The actual value of the ground state energy was calculated by Hulthén in 1938 [1].

The Bethe ansatz works for $S = 1/2$ chain and while it does not work for any $S > 1/2$. This result implies that the chain of $S = 1/2$ Heisenberg spins is an *integrable* system.

Hopefully, the fundamental difference between the quantum and classical nature of spins and the role played by it in determining the ground state energy has been sufficiently impressed in the discussion so far. However, it is not just the ground state energy which is modified, the nature of the elementary excitations in these systems as well as the possibility of realization of new exotic phases, all make the study of low dimensional quantum magnets very interesting.

1.3 The $S = 1/2$ Heisenberg Chain²

While we briefly discussed the 1D Spin-Half Chain, it will serve us well to discuss a little more on this system as it constitutes the most important paradigm of low-dimensional quantum magnetism. It helps us understand various scenarios such as broken symmetry and the emergence of incommensurate phases, gapped and gapless excitation continua etc.

The Hamiltonian for this model is,

$$\mathcal{H} = J \sum_n \left[\frac{1}{2} (S_n^+ S_{n+1}^- + S_n^- S_{n+1}^+) + \Delta S_n^z S_{n+1}^z \right] \quad (1.20)$$

The term,

$$\frac{1}{2} (S_n^+ S_{n+1}^- + S_n^- S_{n+1}^+)$$

is called the transverse part of the Hamiltonian. This term acts as a spin interchange operator as it simply interchanges two oppositely aligned spins ($|\uparrow\downarrow\rangle \rightleftharpoons |\downarrow\uparrow\rangle$).

For different values of Δ , there exist different phases of the 1D chain which are briefly discussed below.

1.3.1 Ferromagnetic Phase

For $\Delta < -1$, the XXZ chain exists in the ferromagnetic Ising phase, with all the spins aligned along $+z$ or $-z$ direction. This phase is representative of a phase with broken symmetry as it does not exhibit the discrete symmetry of spin inversion $S^z \rightarrow -S^z$. The application of an external magnetic field results

²The discussion in this section is based extensively on the review of 1D Quantum Magnetism by Mikeska and Kolezhuk [2]

in an additional energy contribution, however the wavefunctions of the system are not modified.

The low-lying excitations of the ferromagnetic phase are *magnons* which obey the dispersion relation (for any arbitrary S),

$$\epsilon(q) = 2JS(1 - \cos(q) - (\Delta + 1)) + 2g\mu_B HS \quad (1.21)$$

These states are *exact* eigenstates of the XXZ Hamiltonian. In zero field the excitation spectrum has a gap at $q = 0$ of magnitude $|\Delta| - 1$ for $\Delta < -1$. For $\Delta = -1$, the discrete symmetry of spin reflection generalizes to the continuous rotational symmetry and the spectrum becomes gapless.

While the ground state for $\Delta < -1$ exhibits long-range order, the low-lying excitations ensure that there is no long range order at any finite temperature.

1.3.2 Néel Phase

For $\Delta > +1$, the XXZ chain exists in the antiferromagnetic Ising or Néel phase with broken symmetry and one of the two possible ground states. The period of the spin lattice becomes $2a$, and the states have to be described in the reduced Brillouin zone with wave vectors $0 \leq q \leq \pi/a$. Although, $S_{Total}^z = 0$ for the ground state, nevertheless, the sublattice magnetization defined by,

$$S_{sublattice}^z = \sum_{n=odd(even)} S_n^z \quad (1.22)$$

has a finite value.

However, quantum fluctuations prevent the order from being complete since the sublattice magnetization does not commute with the XXZ Hamiltonian, which was true for the ferromagnetic phase.. The elementary excitations for this phase are described as domain wall states, where a single spin flip corresponds to two domain walls. Each of these domain walls mediate between two different Néel states. Although, these domain wall states are not eigenstates for finite values of Δ^{-1} , it is possible to obtain approximate solutions in the limit $\Delta^{-1} \ll 1$ using a perturbative expansion. Thus, the excitation spectrum in the first order in Δ^{-1} [42] is given by,

$$\omega(q, k) = \Delta + 2 \cos q \cos 2\phi \quad (1.23)$$

$$= \epsilon(q/2 + \phi) + \epsilon(q/2 - \phi) \quad (1.24)$$

where,

$$\epsilon(k_i) = \frac{\Delta}{2} + \cos 2k_i \quad (1.25)$$

q is the total momentum and takes the values $q = \frac{2\pi l}{N}$ with $l = 1, 2, \dots, N/2$, while $k_i (i = 1, 2)$ is the individual momentum of each domain wall excitation. ϕ is essentially a relative momentum and for $S_{tot}^z = \pm 1$ takes the values $\phi = \frac{m\pi}{N+2}$

with $m = 1, 2, \dots, N/2$. The precise values reflect that the two domain walls are not interpenetrating. The two domain walls propagate independently with momenta k_1 and k_2 , which is reflected in the fact that the relative momentum ϕ can take from a range of values. These domain walls were first described as magnetic soliton-like excitations by Villain [41]

1.3.3 The Isotropic Heisenberg Chain

The point $\Delta = 1$, corresponds to the isotropic Heisenberg antiferromagnet. The ground state energy of the Isotropic Heisenberg Chain is given by,

$$E = -NJ \ln 2 \quad (1.26)$$

The asymptotic behaviour of the static spin correlation function is given by,

$$\langle 0 | S_n \cdot S_0 | 0 \rangle \propto (-1)^n \frac{1}{(2\pi)^{3/2}} \frac{\sqrt{(\ln n)}}{n} \quad (1.27)$$

The uniform susceptibility at the HAF point is given by [11],

$$\chi(T) = \frac{n_s^2 g^2 \mu_B^2}{\pi^2 J} \left(1 + \frac{1}{2 \ln(T_0/k_B T)} + \dots \right) \quad (1.28)$$

where $T_0 \approx 7.7J$, g is the Lande g-factor, n_s is the number of spin chains per unit cell and μ_B is the Bohr Magneton. This singular behaviour of the spin chain susceptibility as $T \rightarrow 0$ has been observed experimentally in Sr_2CuO_3 and SrCuO_2 [12]. Another expression for the susceptibility of the isotropic Heisenberg chain derived using the series expansion method by Johnston *et al* [13],

$$\chi(T) = \frac{N_A g^2 \mu_B^2}{4k_B T} \left[\frac{1 + \sum_{n=1}^q \frac{N_n}{(T/J)^n}}{1 + \sum_{n=1}^r \frac{D_n}{(T/J)^n}} \right] \quad (1.29)$$

The elementary excitations of the isotropic Heisenberg chain are spin-half fermions which are formed in pairs and propagate independent of each other and are not interpenetrating. The dispersion relation first derived by Cloizeaux and Pearson [14] is given by,

$$\epsilon(k) = \frac{\pi J}{2} |\sin k| \quad (1.30)$$

This describes the lower bound of the two-spinon continuum (see Figure 1.1). k in Eq.1.30 doubles up as the total momentum (q) and the momentum of a single spinon as the lower bound corresponds to the case where only one spinon propagates while the other remains stationary.

It will be quickly summarized at this stage that any anisotropy in the chain opens a gap which is directly proportional to the magnitude of the anisotropy (Δ). The presence of a gap at $k = 0$ implies that the low-energy spin excitations will be suppressed in such systems.

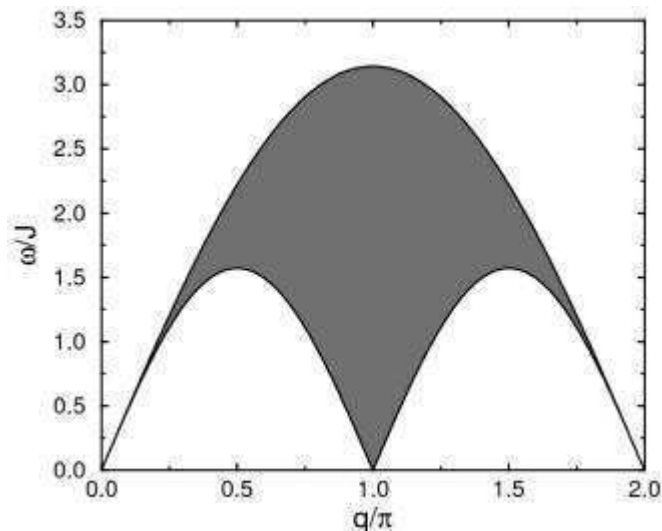


Figure 1.1: The two-spinon-continuum of the isotropic spin 1/2 Heisenberg-chain. The lower bound of the continuum corresponds to the dispersion of one spinon given by Eq. 1.30[15]

With this introduction to the elementary physics of the 1D spin chain, we will proceed to discuss the general idea of order in magnetic systems and discuss the role played by quantum fluctuations in disrupting such order in low dimensional quantum magnets.

1.3.4 Magnetic Order and Quantum Fluctuations

It is interesting to note that early theoretical interest in low dimensional magnetism stemmed from the fact that these systems provided the possibility to obtain exact results which are extremely difficult to obtain in 3D systems. Ising proposed his model with the hope of explaining the origin of spontaneous magnetization in 1D [5]. However, it was found that the model did not show any spontaneous order at any finite temperature. He used this result to erroneously conclude that there is no spontaneous order in 2D and 3D magnets, despite experimental evidence pointing to the contrary. Onsager subsequently proved that the 2D Ising Model indeed shows spontaneous order [6].

In order to fully comprehend the role played by dimensions of the magnetic system, we need to first have a clear picture of an ordered system. For 3D magnetic systems, countless experiments have revealed the emergence of long-range order below a certain *critical temperature*, T_c . This is conveniently revealed by the *order parameter* known as *magnetization*, which attains a finite value below T_c . Physically, long range order means that the relative orientation of the spins even at very large distances is fixed, this information is contained in a very

important function known as the *spin-spin correlation function*.

How the spins actually orient depends crucially on the nature of the coupling. In general, the orientation of the spins change from one lattice site to the next. To make this clear, consider the case of a Bravais lattice. For this lattice the spins order in a helical arrangement as shown in Figure 1.2. The helical configuration is characterised by a pitch vector Q . The correlation function is given by,

$$\langle S_i \cdot S_j \rangle \propto M_s^2 \cos(Q \cdot (R_i - R_j)) \quad (1.31)$$

where M_s is the staggered magnetization.

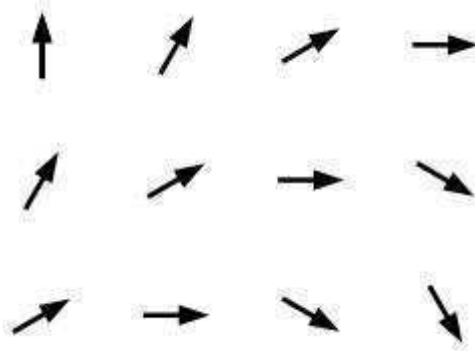


Figure 1.2: Helical Order

The pitch vector Q is given as the minimum of the Fourier transform $\vec{j}(q)$ of the coupling constants.

This helical configuration includes the ferromagnetic alignment ($Q = 0$) and antiferromagnetic alignment ($Q = (\frac{\pi}{a}, \frac{\pi}{a}, \frac{\pi}{a})$) as special cases on a cubic lattice of side a .

The discussion so far has been on the classical limit, where S is treated as a classical three dimensional vector. In the quantum case, apart from thermal fluctuations which effectively reduce M_s at finite temperatures, we also need to take into account additional contribution from *quantum fluctuations* which extend down to $0K$.

At this point we must mention a very important theorem due to Mermin and Wagner [10], which states that *in 2D systems with continuous symmetry of the spins long range order is not possible at any finite temperature, while in 1D systems with continuous symmetry of the spins there is no long-range order down to absolute zero due to the quantum fluctuations present in the system.*

A major consequence of the presence of long range order is the presence of low-energy hydrodynamic fluctuations. In order to account for these low-energy excitations, the *linear spin wave theory* was proposed by Anderson for ferromagnets [7] and later on extended to antiferromagnetic systems by Oguchi [8].

Dimension	$\langle \delta S_i^z \rangle$
3D (Simple cubic)	0.078
2D	0.20
1D	∞

Table 1.1: Comparison of $\langle \delta S_i^z \rangle$ for systems of different dimensions

1.3.4.1 Spin Wave Theory

Quantum fluctuations can be treated in the context of a $1/S$ expansion, such that they vanish in the limit $S \rightarrow +\infty$ (the classical limit). A systematic way of performing this expansion is to use the Holstein–Primakoff representation of spin operators in terms of bosonic creation and annihilation operators:

$$S_i^z = S - a_i^\dagger a_i, S_i^+ = a_i \sqrt{(2S - a_i^\dagger a_i)}, S_i^- = a_i^\dagger \sqrt{(2S - a_i^\dagger a_i)} \quad (1.32)$$

Subsequently, the terms of the Hamiltonian need to be classified according to the powers of $1/S$. If we only keep terms upto orders of $1/S$ and $1/S^2$, this approximation corresponds to what is known as *linear spin-wave theory*.

The advantages offered by the spin-wave theory are that it works for many different Hamiltonians and for any number of dimensions, gives approximate results for non-zero temperatures for arbitrary S and gives a simple physical picture of the spin excitations in the system. While it is not possible to give a detailed introduction to the methods of this theory for which the reader is referred to [9]. An important result obtained therein provides a marker on the role played by the quantum nature of the excitations and the fluctuations in determining the behaviour of these systems at low temperatures. Evaluation of the quantum correction $\langle \delta S_i^z \rangle = S - \langle S_i^z \rangle$ for $S = 1/2$ yields the values listed in Table 1.1.

While the values obtained for the 2D and 3D case are in good agreement with the values obtained with more sophisticated methods, the result for the 1D case is unphysical and this problem is known as *infrared divergence*. This indicates that the spin-wave theory is not applicable for small values of S and low dimensions. Therefore, the approximation of the elementary excitations in these systems as classical spin waves turned out to be incorrect and was in need of a revision. The paradox of $S = 1/2$ was resolved when it was realized that the low-lying excitations are not spin waves but soliton-like topological (domain wall) excitations. In the next section the thermal transport properties in the 1D spin chains due to the spinons is discussed extensively.

1.3.5 Geometrical Frustration

The mechanism of frustration is believed to enhance the low-dimensionality in some compounds (for eg. SrCuO_2). The simplest template to understand the

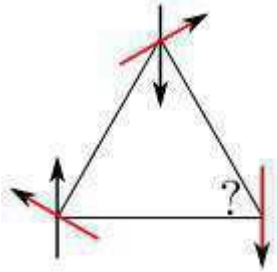


Figure 1.3: A triangle with Ising (black) and Heisenberg (red) spins. The Ising spins are unable to satisfy all nearest neighbour couplings simultaneously, resulting in a ground state degeneracy. In the case of Heisenberg spins, the frustration is relieved by adoption of a coplanar 120° state

origin of geometrical frustration comprises of a triangle with Ising spins at the three vertices. If the spins interact antiferromagnetically with each other, then it is not possible for the system to satisfy all the interactions and attain a unique ground state (see Figure 1.3).

In real materials where spin chains may be approximately realized, the interchain interactions are always present. However, depending on the underlying structure of the lattice these interactions may be frustrated. This leads to the enhancement of the one dimensionality of the spin chains. Moreover, it is believed that due to the fact that a unique ground state configuration cannot be realized in a frustrated system, the quantum fluctuations are actually enhanced, which suppresses the onset of magnetic order.

1.4 Thermal Transport³

1.4.1 Phonons

Any theory which attempts to explain transport of heat must include a description of the motion of the carriers of energy. In metals, free electrons are the foremost contenders, however the material we have investigated is an insulator which eliminates the possibility of heat transport by conduction electrons. The simplest form of motion in a solid comprises of the vibration of the atoms/ions about their equilibrium positions. However, since the atoms/ions are coupled to each other (thus forming the lattice), the individual motion of the atom/ion is not an elementary motion form of the motion of the atoms in a solid. Waves of displacements of the atoms from their equilibrium position can be considered as an elementary form of motion in a solid. The quantum (corpuscular) nature of the waves is revealed due to the existence of the minimum packet of energy

³For the description of the theory of heat transport in low dimensional quantum magnets the references [15, 16, 17] have been quoted extensively.

of the crystal's vibration with a fixed frequency. This makes it possible to propose the existence of specific quasiparticles for the lattice vibrations known as *phonons*.

A crystal comprising of p distinct atoms will have $3p$ dispersion branches. Three of these branches are strongly k -dependent and correspond to sound waves with velocity v_s in the lattice. These are known as the acoustic branches. The remaining $3p - 3$ branches are known as optical branches (so named because they were first determined by optical excitation). These branches are not strongly dependent on k and are normally excited only at high energies which means their contribution to the thermal conductivity at low temperatures is usually negligible and can be ignored.

In an ideal harmonic crystal, the phonon states are stationary, i.e. the distribution of states does not change with time. Therefore, a heat current introduced at any given time will remain unchanged forever which would imply infinite thermal conductivity. In real crystals, however, there are always imperfections which act as extrinsic scatterers. Additionally, the lattice potential always contains terms of higher order, i.e. cubic and higher. These nonharmonic parts of the potential can be treated as small perturbations which describe the interaction of phonons. This constitutes an intrinsic scattering mechanism for the phonons. The presence of these different scattering mechanisms render the thermal conductivity in a solid, finite.

1.4.1.1 Thermal Conductivity due to Phonons

At very low temperatures only a small number of phonons are excited. In a pure defect-free sample they can travel vast distances with only the crystal boundaries limiting the mean free path l_{bd} . The specific heat in Debye approximation depends on temperature as $C \sim T^3$. Therefore, with a constant mean free path l_{bd} , with the Kinetic Theory equation for thermal conductivity,

$$\kappa = \frac{Cvl}{3} \tag{1.33}$$

it follows, that the thermal conductivity also increases as $\kappa_{ph} \sim T^3$.

At temperatures around the peak region, defect scattering is the dominating process in limiting the mean free path l_{defect} and therefore in limiting κ_{ph} .

At higher temperatures the specific heat becomes temperature independent as it attains the Dulong-Petit value $C = 3Nk_B$. At high temperatures the number of phonons increase, alongwith the contribution due to the anharmonic terms. As already mentioned, the extension of the lattice potential to higher orders leads to a scattering mechanism for the phonons, where the order value corresponds to the number of particles involved in the scattering process. A process of third order corresponds to a three particle process, i.e. a phonon from a branch s with a wave vector k is annihilated and two new phonons in the branches s' and s'' , with wave vectors k' and k'' , respectively, are created, or vice-versa. In collisions of quasiparticles the energy is always conserved, so we can write,

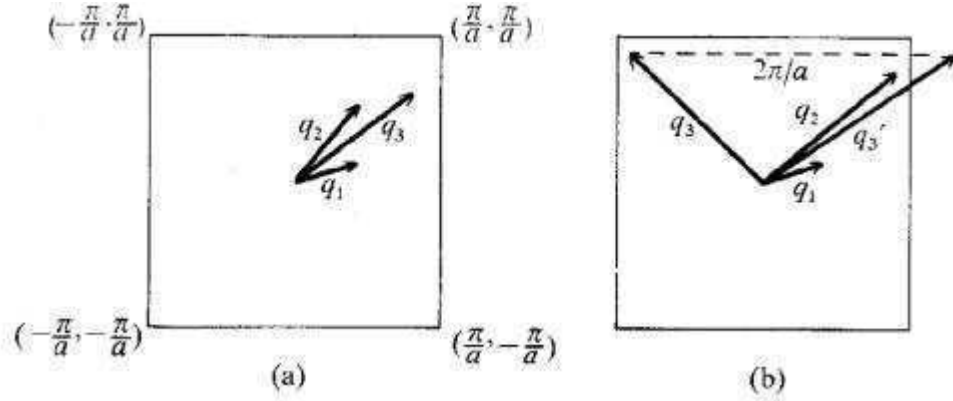


Figure 1.4: Phonon-phonon scattering a) Normal process and b) Umklapp process [18]

$$\omega_s(\mathbf{k}) = \omega_{s'}(\mathbf{k}') + \omega_{s''}(\mathbf{k}'') \quad (1.34)$$

The quasi-momentum may not be conserved in collisions of quasiparticles. However, even if the quasimomentum is not conserved it changes by a definite quantity which is equal to the reciprocal lattice vector, \mathbf{G} . Thus for the quasimomentum we can write,

$$\mathbf{k} = \mathbf{k}' + \mathbf{k}'' + \mathbf{G} \quad (1.35)$$

The collisions in which the quasimomentum is conserved are said to be *Normal processes*, which correspond to $\mathbf{G} = 0$. The normal processes involve scattering of two phonons which results in a third with a wave vector that is still located in the first Brillouin zone (see Figure 1.4(a)).

The scattering processes which violate the conservation of quasimomentum are known as *Umklapp processes*. These are processes in which the scattering of two phonons results in a third with a wave vector that lies outside the first Brillouin zone (see Figure 1.4(b)).

Since such a vector can always be folded back into the first Brillouin zone, it reflects a net change in the direction of the resultant momentum vector after the scattering. The constant reversal in the direction of phonons due to the Umklapp-process leads to the generation of a gradient which opposes the motion of phonons in a given direction.

To determine the nature of thermal conductivity due to phonons at temperatures where the phonon-phonon scattering dominates we must first recognize that in this temperature regime the mean free path of the phonons is inversely proportional to the concentration of the phonons. Therefore according to Bose-Einstein statistics,

$$n_{ph} = \frac{1}{e^{\frac{\hbar\omega}{k_B T}} - 1} \quad (1.36)$$

This leads to,

$$l_{ph} \sim e^{\frac{\theta_D}{2T}} - 1 \quad (1.37)$$

where θ_D is obtained from,

$$\omega = \frac{k_B \theta_D}{2\hbar}$$

In the limiting case of high T , the mean free path is given as,

$$l \sim 1 + \frac{\theta_D}{2T} \sim \frac{1}{T} \quad (1.38)$$

Since at high temperatures the specific heat attains the constant Dulong-Petit value, then according to Eq. 1.33,

$$\kappa_{ph} \sim \frac{1}{T} \quad (1.39)$$

All of the above discussion is summarized in Figure 1.5.

1.4.2 Transport due to Spin Excitations

The Heisenberg chain represents is an integrable model, which means that it is characterised by a macroscopic set of conservation laws [19]. The most relevant conservation from the point of view of transport of heat is the conservation of energy current,

$$[H, j_{th}] = 0 \quad (1.40)$$

This implies that the thermal conductivity is infinite along the chains for $T > 0$ [20]. Similar to the case for phonons, the presence of imperfections and defects remove the integrability of the chain and render the thermal conductivity finite. Additionally the spinon excitations may couple to the phononic excitations and therefore act as an extrinsic scattering mechanism. The precise nature of the mechanism for these interactions is yet to be understood. An approach to deal with the infinity of the thermal conductivity was devised, by treating the magnetic thermal conductivity κ_{mag} as a product of an effective thermal conductivity, D_{th} (Thermal Drude weight) and a delta-function. This can be expressed as a function of frequency as,

$$\kappa_{mag}(\omega) = D_{th}\delta(\omega) + \kappa_{reg}(\omega) \quad (1.41)$$

The regular part of the thermal conductivity is usually considered to be small and neglected. For a real system at zero frequency, the idea is that the weight will be the same but the delta function will broaden due to the extrinsic scattering as,

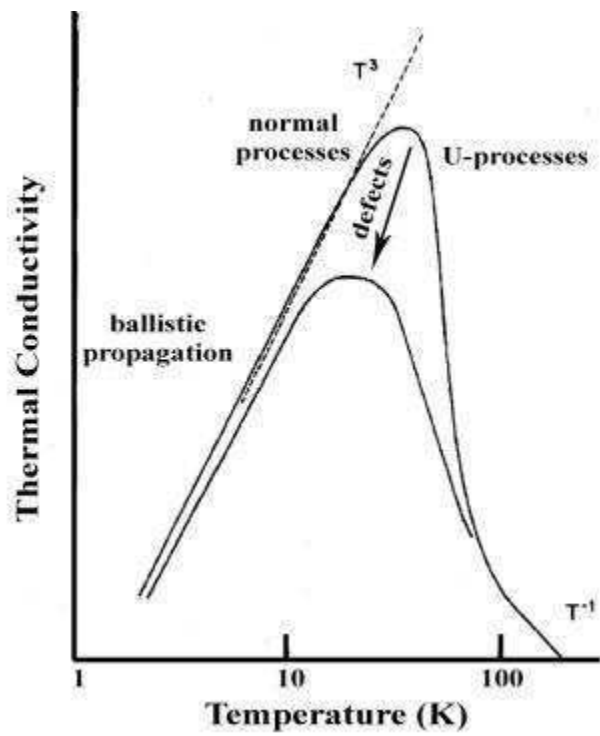


Figure 1.5: Typical behavior of the thermal conductivity of an insulator as a function of temperature. [18]

$$\kappa_{mag}(\omega) = D_{th} \cdot \frac{\tau(T)}{\pi} \quad (1.42)$$

Generally, the temperature dependence of τ is unknown. However, in the regime where the static chain defects are the dominating scattering mechanism, τ will be a constant, independent of temperature.

The thermal Drude weight for the XXZ Model has been calculated by Klümper and Sakai [21]. At low temperatures, the Drude weight increases linearly and may be approximated as,

$$D_{th} = \frac{(\pi k_B)^2}{3\hbar} vT \quad (1.43)$$

Alongwith the broadening proposed in Eq. 1.42, we obtain the low temperature approximation of the magnetic thermal conductivity,

$$\kappa_{mag} = \frac{\pi n_s k_B^2 T}{3\hbar} l_{mag} \quad (1.44)$$

where $l_{mag} = v\tau$ and n_s is the number of spin chains per unit area.

This model cannot reproduce the high temperature behaviour of Sr_2CuO_3 and SrCuO_2 . In these compounds, the maximum of κ_{mag} is at a much lower temperature than the prediction from the Drude weight. It is argued in [16] that this deviation is due to strong spinon-phonon scattering and consequently a strong T dependence of the scattering rate $\tau(T)$.

In experiments, the quantity that is actually measured is κ_{mag} which is then used to calculate l_{mag} . We will use Matthiessen's rule [23, 22], which states that it is possible to define a combined scattering rate which is the sum of the scattering rates from different mechanisms (the assumption is that the different scattering mechanisms are dominant in different temperature regimes). Thus we can write down,

$$l_{mag}^{-1} = l_0^{-1} + l_{sp}^{-1} \quad (1.45)$$

where l_0 describes the T-independent spinon-defect scattering, while l_{sp} (T) accounts for the T-dependent spinon-phonon scattering. At low temperatures the number of spinons is too less for spinon-spinon scattering to play a significant role. For l_{sp} a general Umklapp process with a characteristic energy scale $k_B T_u^*$ of the order of the Debye energy is assumed,

$$\tau_U^{-1} = B\omega^\alpha T^\beta e^{-\frac{\theta_D}{bT}} \quad (1.46)$$

Together with the semi-empirical parameters $\alpha = 0$ and $\beta = 1$ [24, 25] we obtain,

$$l_{mag}^{-1} = l_0^{-1} + \left(\frac{e^{(T_u^*/T)}}{A_S T} \right)^{-1} \quad (1.47)$$

where A_S corresponds to the coupling strength.

1.4.2.1 Spinon-Defect Scattering

A commonly accepted theory which explains the interaction of the spinons with the defects is so far available. In [16], Nikolai discusses a result for a single impurity in a Luttinger liquid. I will briefly present the main results of that discussion. Treating the Hamiltonian as a perturbation the overall temperature dependence comes out as,

$$\kappa_{mag}(T) \sim T^{2/g-1} \quad (1.48)$$

for $g > 0.5$. The generalization to the bulk disorder case is a highly non-trivial problem. A solution has been found by Li and Orignac [26]. They find,

$$\kappa(T) \sim T^{3-g} \quad (1.49)$$

This implies a different T-dependence for the non-interacting case.

1.4.2.2 Spinon-Phonon Coupling

A method, devised by Chernyshev and Rozhkov [27, 28] takes spinon-phonon and spinon-defect scattering into account. It is proposed, that spinons are mainly dissipated by scattering on phonons, which in turn relax their momentum via an Umklapp process. According to the assumptions, the results for the temperature dependence of κ_{mag} is valid in the limit of weak spin-lattice coupling and fast spin excitations. The results obtained by them for different temperature regimes are,

$$\begin{aligned} \kappa_{mag} &\sim T^2, T \ll T_m \\ &\sim T^{-1}, T_m \ll T \ll \frac{\theta_D}{4} \\ &\sim T^0, T \gg \frac{\theta_D}{4} \end{aligned}$$

where T_m is the crossover temperature between the impurity and phonon scattering dominated regimes.

However, these relations do not work for SrCuO₂. An additional transport mechanism called the spinon-phonon drag was proposed. The temperature dependence of this drag contribution is discussed in detail in [29]. The drag conductivity at low temperatures is given by,

$$\kappa_{drag} \sim T^{2+D_s+m} \quad (1.50)$$

where D_s represents the dimensionality of the spin system and m depends on the details of the spin-phonon coupling, which, for standard coupling should result in $m = 3$ according to [29]. Therefore, the expected proportionality of $\sim T^6$ is subleading, with regard to the previously discussed mechanisms.

For very high temperatures, the drag conductivity reduces like the phononic conductivity,

$$\kappa_{drag} \sim 1/T \quad (1.51)$$

The spinon-phonon drag can only occur in sufficiently pure systems.

Another approach [30] to understand the coupling of the spinons to the phonons leads to the following dependence on T ,

$$\kappa_{mag} \sim e^{T^*/T} \quad (1.52)$$

where T^* is predicted to be close to $\theta_D/2$. This effectively reproduces Eq. 1.47

1.5 The Quasi-1D Spin Chain Compound SrCuO₂

Strictly speaking, all the systems are three dimensional (3D), however it is possible that the couplings in one or two dimensions are much stronger than other couplings. This effectively renders the system 1D or 2D in character. This is precisely the case for cuprates, especially Sr₂CuO₃ and SrCuO₂ which are recognized to be the best realizations of a 1D quantum magnet.

1.5.1 Structure

SrCuO₂ is orthorhombic in structure with Cmcm symmetry (see Figure 1.6). The main structural units which determine the physical properties of this compound are the CuO₂ zigzag ribbons which extend along the crystallographic c -direction. Each ribbon is composed of corner-sharing CuO₂ chains. The straight Cu-O-Cu bonds of each double chain structure result in very large antiferromagnetic exchange $\frac{J}{k_B} \approx 2100 - 2600K$ of the $S = 1/2$ spins of the Cu²⁺ ions as predicted by Goodenough and Kanamori [49, 48]. The 90°Cu-O-Cu bonds between two Cu ions on adjacent chains results in a much weaker ferromagnetic coupling, $\frac{|J'|}{k_B} \approx 200 - 500K$. In the zigzag configuration, the nearest neighbour interaction is the weak 90°ferromagnetic interaction, while the next nearest neighbour interaction is the strong antiferromagnetic interaction. Irrespective of the sign of the NN interaction, the antiferromagnetic nature of the NNN interaction results in frustration in the system. The inherent frustration alongwith quantum fluctuations are believed to be responsible for the suppression of 3D long range order in SrCuO₂ down to 2K. Therefore, at higher temperatures it is possible to approximate the two chains comprising the ribbon to be magnetically independent.

The zig-zag chain with frustrated NNN interaction offers the possibility of realizing many exotic phases depending on the relative strength of the couplings. Some of them are summarized in Figure 1.8 [31]. The region of our interest in that diagram is near the upper vertex, since in our system $J_2 \gg J_1$ and J_2 is

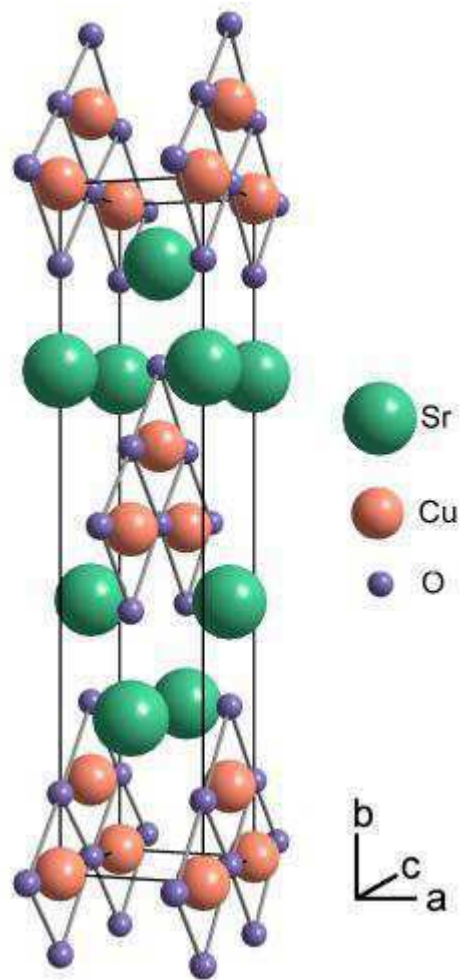


Figure 1.6: Crystal structure of SrCuO₂. The lattice constants are $a = 3.56 \text{ \AA}$, $b = 16.32 \text{ \AA}$, $c = 3.92 \text{ \AA}$ [16]

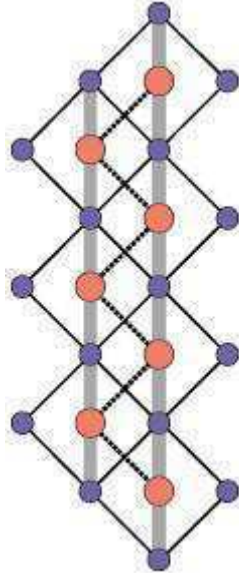


Figure 1.7: The double chain ribbon of CuO_2 [16]

negligible. The shaded regions represent those where open questions need to be addressed.

At large J_2 the problem is one of chains with competing ladder and frustrated couplings. The ladder coupling opens a gap Δ linear in J'_2/J_2 to the nondegenerate state. The zigzag chain coupling opens an exponentially small gap $\Delta \sim e^{-J_2/J_1}$ to the multiply-degenerate state [43]. How each bond type affects the gapped state established by the other is unknown, as both gaps may close, leaving some intermediate phase, or there may be a crossover between the gapped states.

This schematic phase diagram in Figure 1.8 has been obtained for the system shown in Figure 1.9 [31]

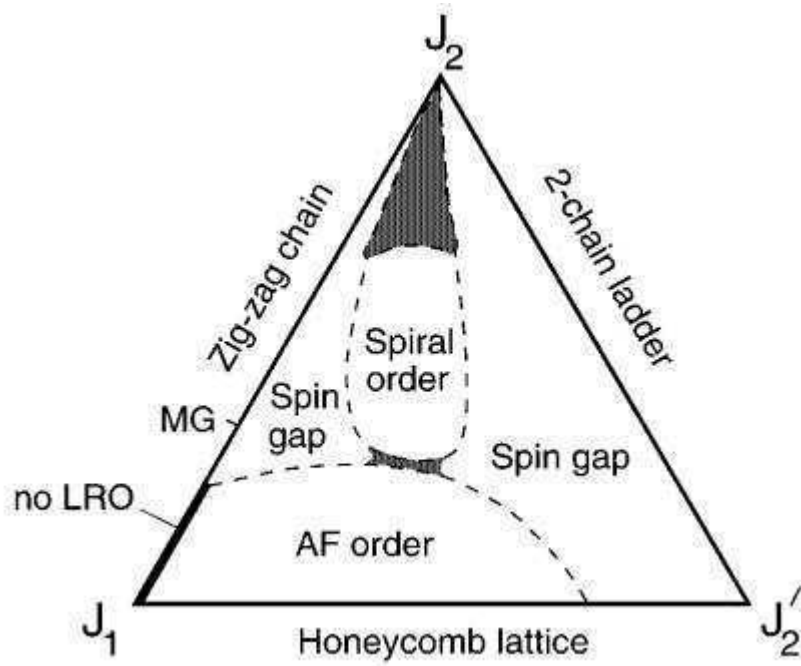


Figure 1.8: A schematic phase diagram of the frustrated coupled ladder system (Normand reference). The region of our interest is the area near the upper vertex along the left side.[31]

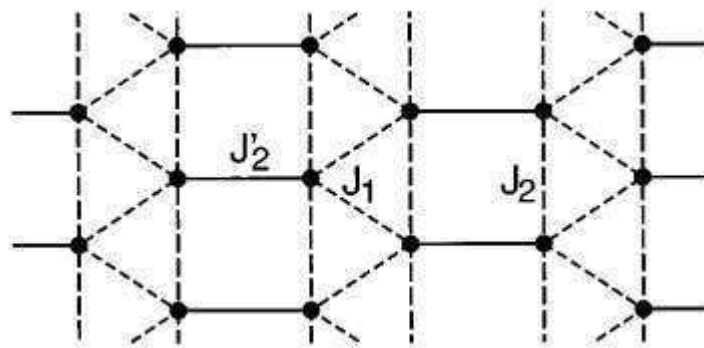


Figure 1.9: A schematic representation of the frustrated coupled ladder system [31]

Part II

Synthesis of the Crystals

Chapter 2

Crystal Growth¹

2.1 Principles of single crystal growth

Figure 2.1 shows a schematic binary phase diagram of a two component system with limited miscibility in the solid state, which consists of three discrete solid phases, α , β and γ . The first two phases represent the homogeneity region of the components A and B, respectively, with small amounts of the opposite component in solution. γ represents the homogeneity region of the chemical compound X, which is described by the formula $A_{1-x\pm\delta}B_{x\mp\delta}$, where δ describes a doping deviation. The compound X shows an incongruent melting behavior, since it decomposes at the peritectic temperature into the B-doped α -phase P_2 and a melt of the composition C_T .

The intersection points of the isotherms with the liquidus and solidus lines indicate which liquid and solid phases with compositions C_L and C_S are in equilibrium. The respective temperature specifies the melting temperature T_M , which is a function of the liquid composition. The ratio between the liquid and solid compositions is called the distribution coefficient: $k = \frac{C_S}{C_L}$.

The concentration of the solute in the melt is higher than in the solid phase, when $k < 1$. This is the case for all the phases shown in Figure 2.1, for instance, if we consider the component B as the solute in the phases α and γ , or component A as the solute in the phase β . If a melt with a solute concentration C_L is cooled down, solid material with a lower solute concentration C_S solidifies at the liquidus line, this leads to a progressive enrichment of the solute in the melt. For the case of directional solidification of a melt, realized by translation of a temperature gradient along an elongated (e.g. cylindrical) melt volume, as shown schematically in Figure 2.2, the change of the solute concentration in the melt reads [34, 33],

$$C_L(g) = C_0 \cdot (1-g)^{(k_0-1)} \quad (2.1)$$

¹For the principles of the crystal growth, the text [15] has been extensively quoted in this chapter.

where g is the quotient of the solidified volume V_S and the total volume V_{Total} , i.e. $g = V_S/V_{Total}$, and C_0 is the initial concentration of the liquid phase. For the sake of simplicity the distribution coefficient was set to a constant value, $k_0 = k = C_S/C_L$, a situation which is realized for instance by considering straight liquidus and solidus lines (shown as inset in Figure 2.1). For $k_0 \neq 1$ equation 2.1 describes a continuous change of the solute concentration in the melt (a solute enrichment for $k_0 < 1$) and, according to $C_S = k_0 \cdot C_L$, in the solidified material as well (see Figure 2.3). It is possible to reduce this effect by making g small, i.e. by growth of small amounts of material out of comparatively large melt volumes.

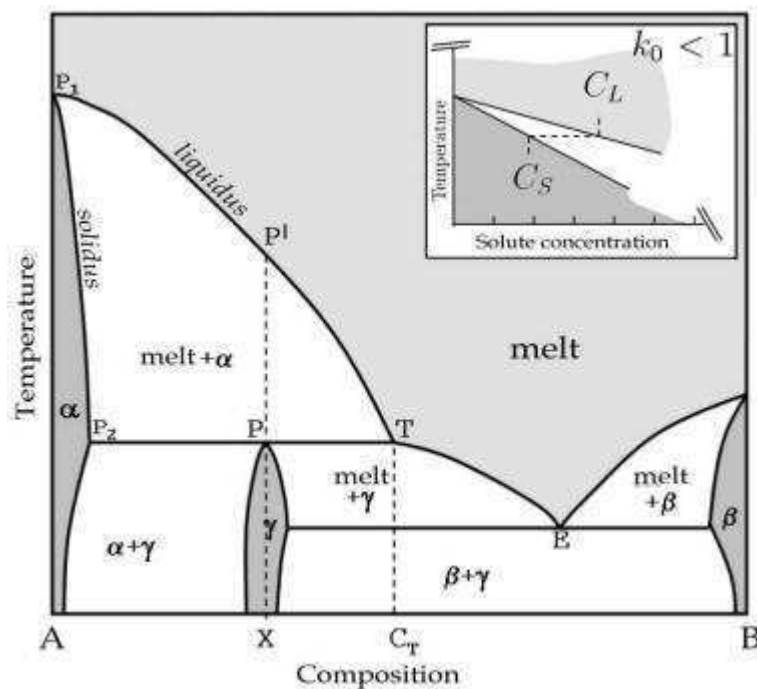


Figure 2.1: Example of a binary phase diagram with an incongruent melting phase γ . The **inset** shows the distribution coefficient set constant by assuming straight liquidus and solidus lines. [15]

2.1.1 Travelling Solvent Floating Zone Technique

A method that can avoid the appearance of concentration gradients during the solidification process is the so called zone melting technique, which involves the translation of the molten zone along a solid rod, as shown in Figure 2.2b. The zone, created by local heating, is confined to an extension, l , much smaller than the total rod length L . The translation of the zone along the rod causes the material to melt at one zone boundary and subsequently recrystallize at the

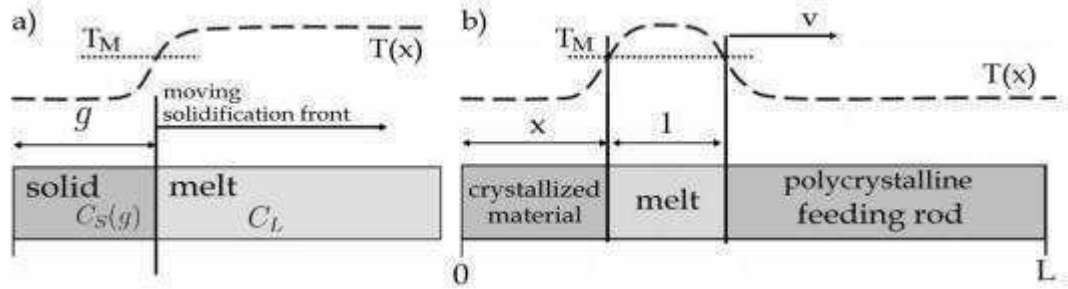


Figure 2.2: Schematic representations of a directional solidification (a) and the zone melting technique (b). T_M denominates the melting temperature and $T(x)$ the temperature profile (indicated by the dashed lines.)[15]

solidification front. The principles of the zone melting were established 1952 by Pfann [32].

The growth of a crystal of the incongruently melting compound X, shown in the phase diagram of Figure 2.4, is done from a melt of different (constant) composition C_T along the peritectic line PT. This can be done by the zone melting technique. In the growth of an incongruent system the melt plays the role of a solvent, for this reason the technique is also known as ‘*The Travelling Solvent Zone Method*’. Using this technique it is possible to realize crucible-free growth by taking advantage of the surface tension of the melt to confine it between two vertical rods (feed rod and seed). This method is better known as the ‘*Travelling Solvent Floating Zone Method*’. It is highly suited for crystal growth for a wide range of compounds with high melting temperature and/or high reactivity.

2.1.1.1 Stabilization Process

The molten zone is created by locally heating a polycrystalline rod composition X (P^1 in Figure 2.4). By translating the melt zone along the feed rod, material of the A-rich α -phase solidifies at the lower zone boundary, while at the same time material from the feed rod of the composition X melts into the zone. Effectively the zone becomes enriched with component B until it reaches C_T and instead of the phase α , material of the composition X solidifies along the peritectic line PT. Once this situation is reached, no further change of the zone composition takes place, since the feed material and the crystallized material possess identical composition.

The TSFZ-growth (assuming we know the phase diagram) can be initiated from a (solvent) pellet which possesses the correct composition C_T of the peritectic point. This allows the quick establishment of the steady state. It is possible to obtain the phase γ from any melt composition lying between C_T and the eutectic composition. However, it must be emphasised that the exact

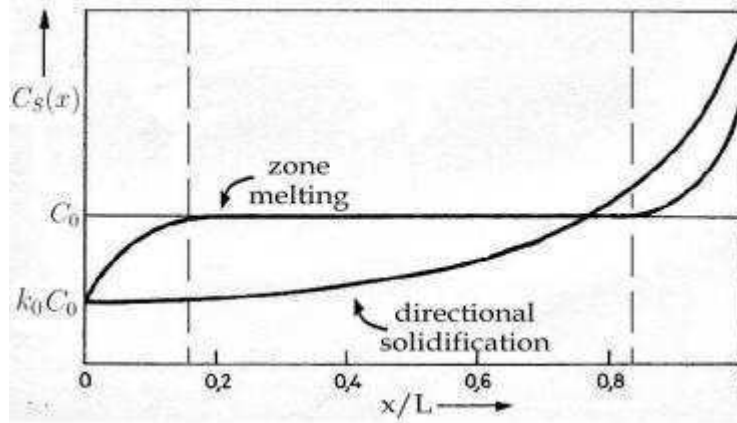


Figure 2.3: Distributions of the solute concentrations $C_S(x)$ for the directional solidification method and zone melting method. [15]

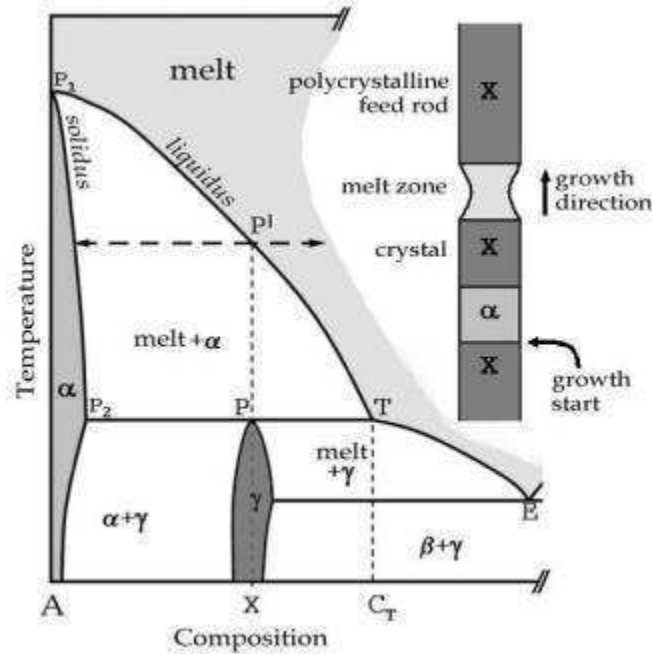


Figure 2.4: Left: Extract of the phase diagram shown in Figure 2.1. Right: Scheme of the first grown phases starting with a melt of composition X

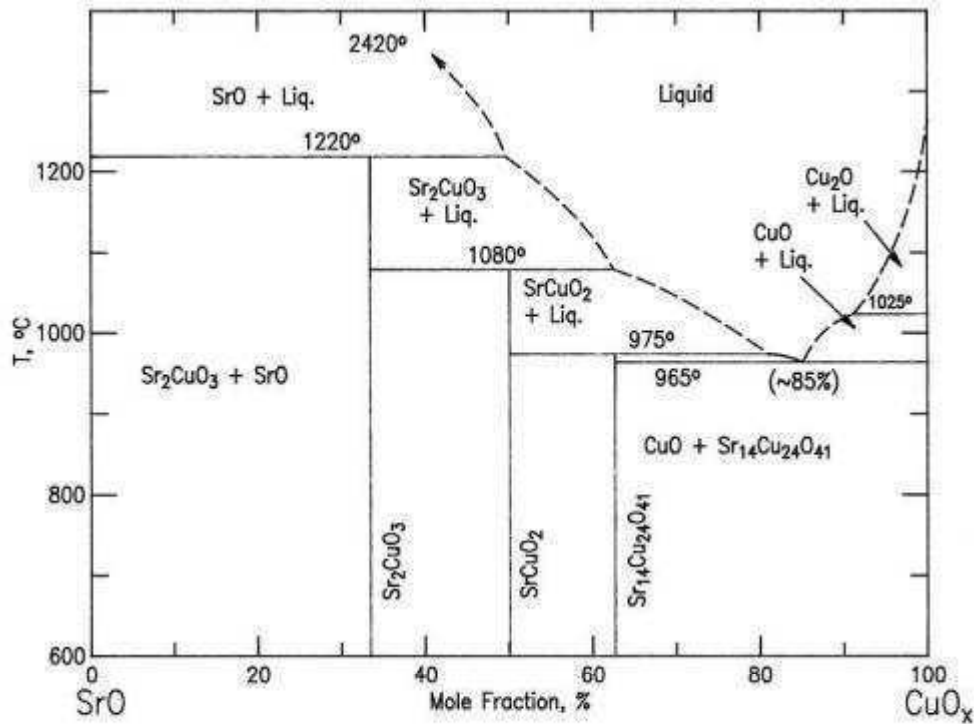


Figure 2.5: Phase diagram of the pseudo-binary SrO-CuO system in air [35]

compound X can only be grown at the peritectic point, since the other intermediate compositions can be obtained during the growth (which is the case for the γ phase shown in Figure 2.4).

2.1.2 Phase Diagram of SrO-CuO Binary System

The phase diagram for the (pseudo) binary SrO-CuO system is shown in Figure 2.5 for air atmosphere at ambient pressure [35]. Under these conditions three ternary solid phases are stable, namely Sr_2CuO_3 , SrCuO_2 and $\text{Sr}_{14}\text{Cu}_{24}\text{O}_{41}$. All three of them exhibit an incongruent melting behavior. SrCuO_2 decomposes at 1080°C into Sr_2CuO_3 and a melt with a Sr to Cu ratio of approx. 4 : 6. Both Sr_2CuO_3 and SrCuO_2 possess rather large temperature windows where the solid-liquid equilibrium is present, while for $\text{Sr}_{14}\text{Cu}_{24}\text{O}_{41}$ this temperature window is very small.

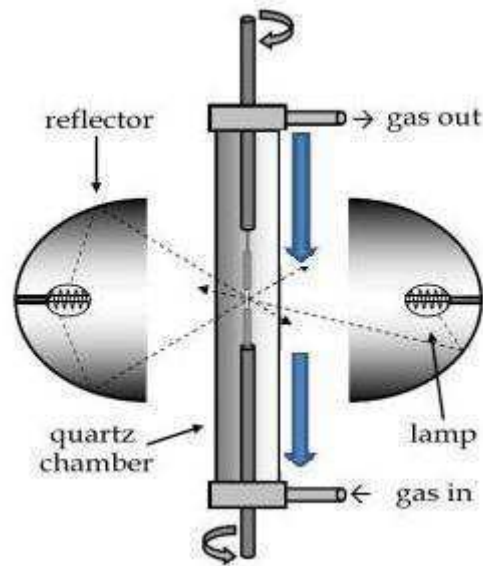


Figure 2.6: A Schematic Representations of the TSFZ-Furnace [15]

2.2 Experimental Realization of the TSFZ-Method

This section addresses some general practical aspects concerning the different stages of the crystal growth of the Co and Zn doped SrCuO_2 .

2.2.1 Furnace for Crystal Growth

For the growth of the strontium cuprates by the travelling solvent floating zone technique a four-mirror optical furnace equipped with four 300W lamps was used (see Figure 2.6). This device can be operated at pressures up to 10 bar of air, oxygen, argon atmosphere and allows flux rates of $100\text{cm}^3/\text{min}$ for oxygen and $1000\text{cm}^3/\text{min}$ for argon, at ambient pressure as well as under pressure. The upper and lower shaft, to which feed and seed rod are respectively attached, can independently perform vertical translations with stable velocities (which correspond to the growth rates) in the range of $0.1\text{--}10\text{mm}/\text{h}$ and rotate in opposite directions with the rates of rotation between 1 rpm to approximately 40 rpm. A video monitoring system which provides a visual feedback via the operating computer allows for direct observation of the crystal growth.

2.2.2 Feed Rod

The success of a crystal growth using the TSFZ method depends directly on the quality of the feed rod. It should have:

- High density

- Constant diameter throughout the length
- High level of homogeneity.

All of these factors together ensure a stable melting zone during the growth process. Any variation of either the rod density, diameter or chemical composition leads to a change in the zone composition which may destabilize the molten zone. The importance of a high density mainly ensures that the liquid from the molten zone does not seep through the pores in the feed rod by capillary action. The homogeneity of the chemical composition throughout the entire rod is also of utmost importance. The rod should be perfectly cylindrical, i.e. with a constant diameter and no curvature along its length. This ensures that there is no off-axis component of rotation during the growth. As much as possible, the feed rod should be accurately centered at the common focus of the lamps, this ensures a regular and homogenous heating and melting of the rod.

To ensure the chemical homogeneity, a great deal of attention needs to be given to the initial mixing and grinding of the precursors. The process of grinding and sintering is repeated over multiple steps as the sintering temperature is gradually increased in steps from $870^{\circ}C$ to $960^{\circ}C$. To ensure the formation of the correct phase regular X-ray phase analysis of the powder was carried out after every sintering step. To ensure a high density of the rod, a special attention was given in the last grinding step to make the powder grain size as small as possible.

The feed rods were prepared by putting the finely ground powder after the final sintering at $960^{\circ}C$ in rubber tubes which were periodically shaken while putting the powder in to ensure uniform density of powder. Once the tube is filled, it is closed with a silicon cap and the air is evacuated using a syringe attached to a vacuum pump. The powder is pressed inside the rubber tube in a hydraulic press under a pressure of upto 700 bar. After the rods are prepared using the hydraulic press, they were put in for a final sintering at $995^{\circ}C$ for a duration of 24 hrs to ensure good homogeneity of the feed rod.

2.2.3 Choice of Solvent

The choice of the solvent depends on the accuracy of the phase diagram, on the estimated peritectic temperature and composition. For all the growths a solvent pellet with a Cu is to Sr ratio of 7 : 3 was used. For the case of Zn and Co doped samples, proportional levels of Zn and Co concentrations were introduced in the pellet composition such that the (Cu+Zn (or Co):Sr) ratio is preserved. The pellet was prepared in the same way as the feed rod and sintered for 24 hrs at $850 - 870^{\circ}C$.

For the growth, the pellet is first fused onto the feed rod which is fixed onto the lower shaft. Subsequently, the feed rod is suspended from the upper shaft and the growth is initiated with the seed fixed on the lower shaft.

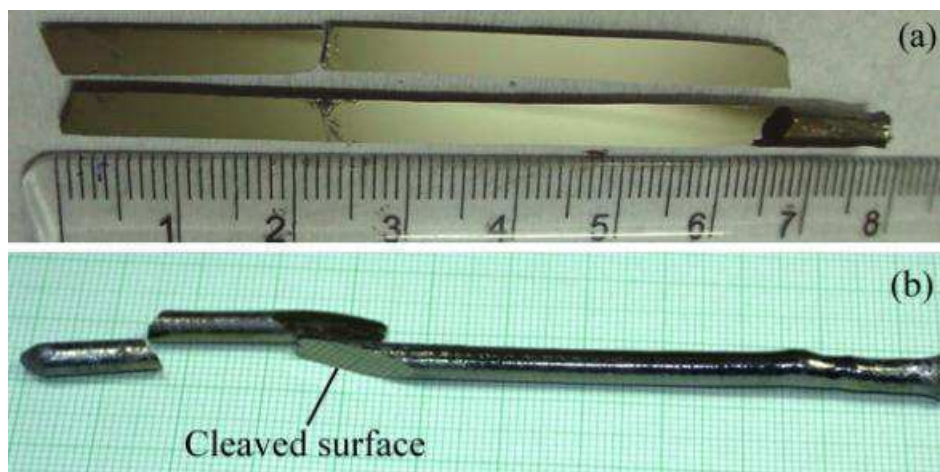


Figure 2.7: Pictures of cleaved single crystals of: a) SrCuO_2 and b) $\text{SrCu}_{0.9975}\text{Co}_{0.0025}\text{O}_2$. The mirror-like cleaved surfaces are the crystallographic ac -plane

2.2.4 Growth of Co and Zn doped SrCuO_2 ²

The polycrystalline powder of single phase of pure SrCuO_2 , $\text{SrCu}_{0.995}\text{Zn}_{0.005}\text{O}_2$, $\text{SrCu}_{0.99}\text{Zn}_{0.01}\text{O}_2$, $\text{SrCu}_{0.9975}\text{Co}_{0.0025}\text{O}_2$, $\text{SrCu}_{0.995}\text{Co}_{0.005}\text{O}_2$ and $\text{SrCu}_{0.99}\text{Co}_{0.01}\text{O}_2$ were prepared by the standard solid state reaction process by heating the stoichiometric mixture in air at 850°C upto 975°C in steps. As precursors for the synthesis very fine powders ($< 10\mu\text{m}$) of SrCO_3 (Sigma-Aldrich: 99.9 %), CuO (Sigma-Aldrich: 99% for the pure compound and Alfa-Aesar: 99.995 %) was used for all the doped compounds), ZnO (Sigma-Aldrich 99.99 %) and for Co doped samples Co_3O_4 (Sigma-Aldrich) was used. The powders of the starting precursors were ground thoroughly using a mortar and pestle in their stoichiometric ratio (SrCO_3 was preheated and dried over night at 900°C before weighing). The ground powder was subsequently calcined in an alumina crucible at 850°C . In each subsequent step upto 975°C , the powder was ground thoroughly for an average duration of 35-40 minutes and put for sintering for an average duration of 12-24 hrs. The phase analysis of the final product was done using powder x-ray diffraction (Bruker D8 Advance Powder X-Ray Diffractometer). If additional phases were found, the sintering step at 975°C was repeated until a single-phase powder was obtained. After the single phase powder was obtained, it was filled in rubber tubes and cold-pressed under 700 bar pressure to prepare the feed rods (about 5 mm in diameter and 80 – 100 mm in length) for the growth. These rods were subjected to a final heat treatment at 995°C to ensure excellent homogeneity. The solvent disk was prepared separately in the form of

²Details of the growth of all the samples of Co and Zn doped SrCuO_2 are currently in the process of submission to the *Journal of Crystal Growth*

a pellet of thickness 3 – 4 mm and of the same diameter as that of the rods. The pellet composition was taken as SrO:CuO=3:7 (molar ratio). For the doped samples, a proportional amount of dopant was introduced to replace CuO in the solvent disks. For the growth, the solvent disks were first fused to the feed rod before initiating the growth. All the crystals were grown under a constant O₂ flow. The growth rates were maintained at 0.7 – 1mm/h to obtain a stable float zone throughout the growth. The rate of translation of the lower shaft was kept faster than the upper shaft to prevent the rods from touching each other at any time during the growth. The rods were rotated in opposite directions to ensure uniform melting and chemical homogeneity in the float zone.

Part III

Experimental Techniques

Chapter 3

Magnetic Susceptibility and Thermal Transport

3.1 Magnetic Susceptibility¹

Susceptibility and magnetization of the crystals was measured by applying the field along the three different crystallographic directions using a superconducting quantum interference device (SQUID) (Quantum Design-MPMS XL) and a vibrating sample magnetometer (VSM) (Quantum Design- PPMS-Evercool II). The susceptibility and magnetization measurements were done in static magnetic fields upto 7T in magnitude. The different crystallographic directions were identified using a Back Reflection Laue Diffractometer and the measurements were accordingly performed on the samples.

3.2 Thermal Transport Measurement

3.2.1 Principles of Measurement of Heat Transport

The thermal conductivity $\kappa(T_m)$ at a temperature T_m is defined by Fourier's law. The schematic setup depicted in Figure 3.1 shows an experimental realization for utilization of the core of Fourier's Law. A cuboidal sample is glued on one of its small faces of area A to a heat reservoir which is at a temperature T_{surr} . A heat source with a temperature $T_1 > T_0$, in the form of a resistive heater, is glued onto the opposite face. This leads to the establishment of a steady thermal current j_i through the sample. The heater power P_h is determined by supplying a constant electrical current I_h and measuring the voltage drop U_h . Hence the generated thermal current is given as,

¹All the magnetization and susceptibility measurements were carried out by Koushik Karmakar (PhD Student) under the supervision of Dr. Surjeet Singh at IISER Pune

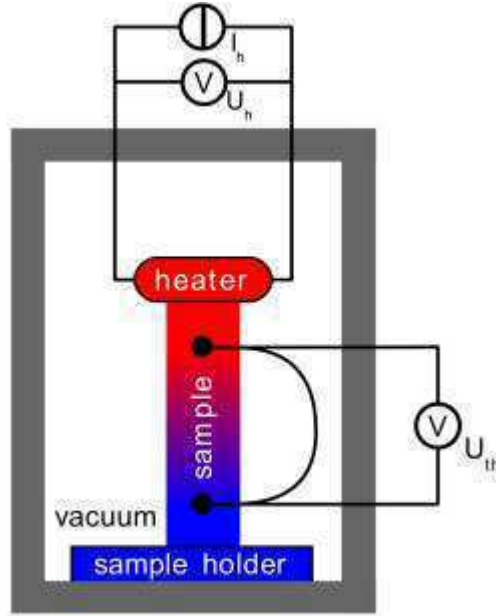


Figure 3.1: Schematic Representation of Real Setup

$$j_i = \frac{P_h}{A} = \frac{U_h I_h}{A} \quad (3.1)$$

This heat current will give rise to a temperature gradient ∇T that is measured in form of a thermal voltage U_{th} by a differential thermocouple with its junctions placed on the sample at a distance of l from each other on the sample. The temperature difference between both contacts can be obtained by $\Delta T = \frac{U_{th}}{S_{th}}$, where S_{th} is the temperature and magnetic field dependent thermo power of the thermocouple. To get rid of possible background voltages the thermal voltage is measured twice, with and without an applied thermal gradient. Assuming the thermal gradient to be homogeneous throughout the sample one gets,

$$\nabla T_i = \frac{\Delta T_i}{l} = \frac{U_{th}}{S_{th} l} \quad (3.2)$$

The mean sample temperature during the measurement is given by,

$$T_m = T_0 + (d + \frac{l}{2})(\nabla T)_i \quad (3.3)$$

where d is the distance from the heat reservoir to the nearest thermocouple junction. Using this we ultimately obtain the following expression for the measured thermal conductivity:

$$\kappa(T_m) = \frac{U_h I_h}{A} \cdot \frac{S_{th} l}{U_{th}^{on} - U_{th}^{off}} = \frac{P_{h..l}}{A \cdot \Delta T_l} \quad (3.4)$$

Since this method involves the establishment of a stable thermal gradient it is known as the *steady state method* for thermal transport

3.2.2 Experimental Setup

The experimental setup used for the measurement of the thermal conductivity allows for measurement down to 6K. For this purpose, the probe, in which the sample is installed, is immersed into liquid helium. The sample chamber which is present at the bottom side of the probe (consult Figure 3.2), is connected by capillaries to a brass stage, which is in direct contact with the liquid helium, allowing a cooling of the sample down to temperatures around 6 K. The heating of the sample chamber is done by means of a heater cup which is made of wound up high resistant manganin wires. An additional inner cup shields the chamber space from eventual radiation of the heater cup. The measurement of the temperature is carried out by using commercial sensors² and a temperature controller³, which controls the current supply to the heater cup. Under steady state conditions, the sample chamber possesses a homogenous temperature distribution and a stability of few mK. The probe can be evacuated down to pressures of 10^{-6} mbar or lower which ensures that there is no loss of heat to the environment by convection.

The samples were glued onto the heat bath at the bottom of the probe using a glue⁴, which was verified in measurements performed earlier to be a good heat conductor [16]. For a successful measurement it is very important that the sample glues well onto the surface of the heat bath.

The thermocouples used for the measurement of the temperature gradient were made using a combination of $\text{Au}_{0.93}\text{Fe}_{0.07}$ and Chromel-P wires. The contact of the thermocouple junctions onto the sample were made using silver paste since silver has a very high thermal and electrical conductivity (this is needed as the thermal gradient across the two junctions sets up a small but finite current along the thermocouple wires which is what is measured by a nanovoltmeter).

3.2.3 Sources of Error

Geometry of the sample and the thermal contacts

The biggest uncertainty in the measurement of thermal conductivity arises from inaccuracies in the determination of the exact dimensions of the sample (the sample, unless cut with precision is never perfectly cuboidal), as well as the uncertainty in the estimation of the distance between the two thermocouple

²CernoxTM Sensors from Lakeshore

³Lakeshore 340 or Lakeshore DRC-93CA

⁴UHU Sekundenkleber

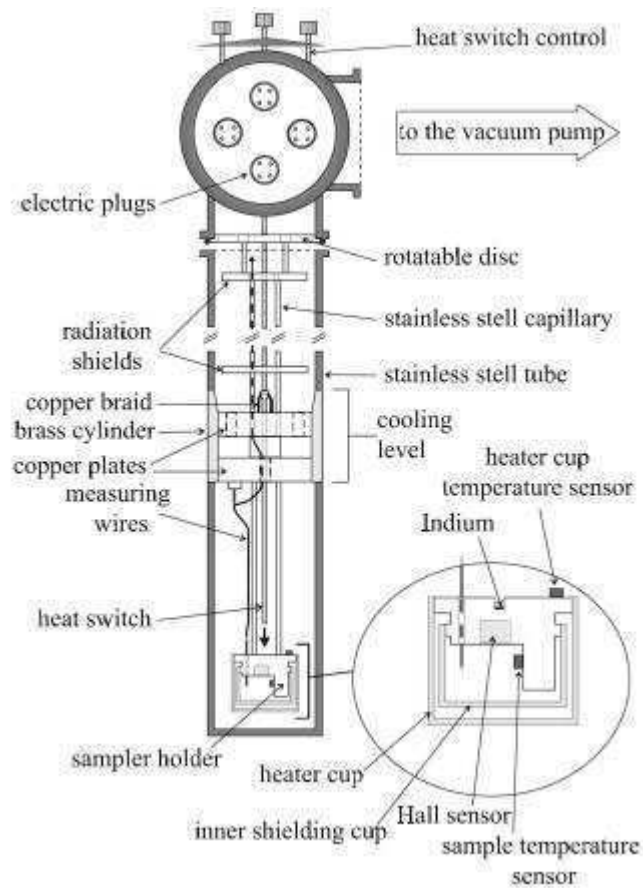


Figure 3.2: Schematic representation of the probe and the sample chamber

contacts. The lower bound for this uncertainty is 10% for a good sample geometry, however this error may be larger. It is difficult to quantify the extent of this error in every measurement. However, since this error exists as an invariant for all the data points in the measurement, it can simply be seen as an overall scaling factor.

Thermocouple

The uncertainty in the thermocouple arises due to uncertainty in the gauge of the thermocouple. This uncertainty is usually smaller than 5%.

Measurement Devices

A high quality heat sensor and temperature controller was used to reduce temperature fluctuations to less than 5mK during the measurement. The thermocouple was monitored by a nanovoltmeter with appropriately shielded cables and for the heater a separate current source and multimeter were used to ensure that all uncertainties of the electrical measurements were smaller than 1% and could be safely ignored

Heat Losses

In the calculation of κ it is assumed that the entire heat from the heater flows through the sample, however this is an idealization. In any real system there will be losses due the three modes of heat transfer in any system: conduction, convection and radiation. The first two are substantially reduced by using extremely thin lead wires to connect the probe head to the sample holder and ensuring a good vacuum in the probe during the measurement. It is not possible to reduce the heat loss due to radiation, but a correction to the thermal conductivity can be made by estimating the amount of heat loss from radiation. This can be done as follows:

The net radiation from a solid at a finite temperature T_{sol} is given by the Stefan-Boltzmann Law:

$$P_{rad} = \epsilon\sigma A(T_{sol}^4 - T_{surr}^4) \quad (3.5)$$

where A is the total surface area of the sample, σ is the Stefan-Boltzmann constant and ϵ the emissivity ($= 1$ for a perfect black body). If the temperature of the solid is, $T_{sol} = T_{surr} + \delta T$ with $\delta T \ll T_{surr}$, then we can write for P_{rad} in the first approximation,

$$P_{rad} = 4\epsilon\sigma AT_{surr}^3\delta T \quad (3.6)$$

Since the heater is kept at a constant temperature, the above equation may be used to estimate the loss due to radiation by integrating the radiation loss over the entire sample surface. Performing the integration yields,

$$P_a = 4\sigma[(w+h)\epsilon_S \frac{L^2}{l} + S_h \epsilon_h \frac{L}{l}] T_{surr}^3 \delta T \quad (3.7)$$

The new variables introduced in this equation are the dimensions of the sample (L length, w width, h height), the surface area of the heater S_h , the emissivities: ϵ_{sol} of the sample and ϵ_h of the heater. With equation for the radiation loss the actual heat flow through the sample P_0 can be calculated as $P_h - P_a = P_0$. Hence Eq. 3.4 can be written down as comprising of two contributions, one describing thermal conduction and an additional term for the radiation loss.

$$\kappa(T_m) = \frac{P_0 \cdot l}{A \cdot \Delta T_l} + \frac{P_a \cdot l}{A \cdot \Delta T_l} = \kappa_0(T_m) + \frac{P_a \cdot l}{A \cdot \Delta T_l} \quad (3.8)$$

The corrected thermal conductivity is therefore given as,

$$\kappa_0(T_m) = \kappa(T_m) - C T_0^3 \frac{l}{A} \quad (3.9)$$

Thus the correction due to radiation losses will only be appreciable at higher temperatures, at low temperatures the error due to neglect of the radiation loss can be estimated to be around 0.05% to 3%, which is well below the error due to the estimation of the geometry of the sample.

Assumption of Isotropy of κ_{ph}

It must be mentioned here that there is an additional contribution to the error at low temperatures due to the assumption that the phononic contribution to the thermal conductivity is identical along the spin chain and perpendicular to the chain. It is not possible to estimate the error due to this assumption, however qualitatively it can be said that the magnitude of this error is higher at lower temperatures (temperatures around the peak of the thermal conductivity) since at higher temperatures Umklapp-scattering is expected to reduce the thermal conductivity thus making the difference due to anisotropy negligible at high temperatures.

An upper limit to the combined error at low temperatures due to all the sources discussed above is placed at 30% of the measured value in [40].

Part IV

Results and Discussions

Chapter 4

Magnetic Susceptibility and Transport Properties

4.1 Magnetic Susceptibility¹

The susceptibility for all the compositions was analyzed using the relation,

$$\chi(T) = \chi_{core} + \chi_{CW} + \chi_{ChainBreaks} + \chi_{Chain} \quad (4.1)$$

$\chi_{core} = \chi_0 + \chi_{VV}$ (χ_0 is the constant diamagnetic contribution while χ_{VV} is the Van Vleck contribution to paramagnetism which is independent of temperature)

$\chi_{CW} = \frac{C}{T-\theta}$ = Curie Weiss Law (Accounts for the paramagnetic contribution due to impurities (mostly attributed in cuprates to the presence of extra interstitial oxygen ions))

$\chi_{ChainBreaks} = \frac{N_A g^2 \mu_B^2 S(S+1)}{3k_B} \frac{p}{12 \ln(2.9J/T)}$ = Contribution from free paramagnetic moments induced around a break in the chain [36]

$\chi_{Chain} = \frac{N_A g^2 \mu_B^2}{4k_B T} \left[\frac{1 + \sum_{n=1}^q \frac{N_n}{(T/J)^n}}{1 + \sum_{n=1}^r \frac{D_n}{(T/J)^n}} \right]$ = Susceptibility of an isotropic Heisenberg spin chain obtained from series expansion [13]

The susceptibility data obtained for the pure compound was found to be in good agreement with previously reported measurements [12]

¹All the measurements and analysis were done by Koushik Karmakar (PhD student) as part of his research work at IISER Pune under the guidance of Dr. Surjeet Singh and therefore only a few representative data for Co doped samples which are proposed to be submitted in a paper to the *Journal of Crystal Growth* are discussed in this thesis to assist in the formation of a holistic picture.

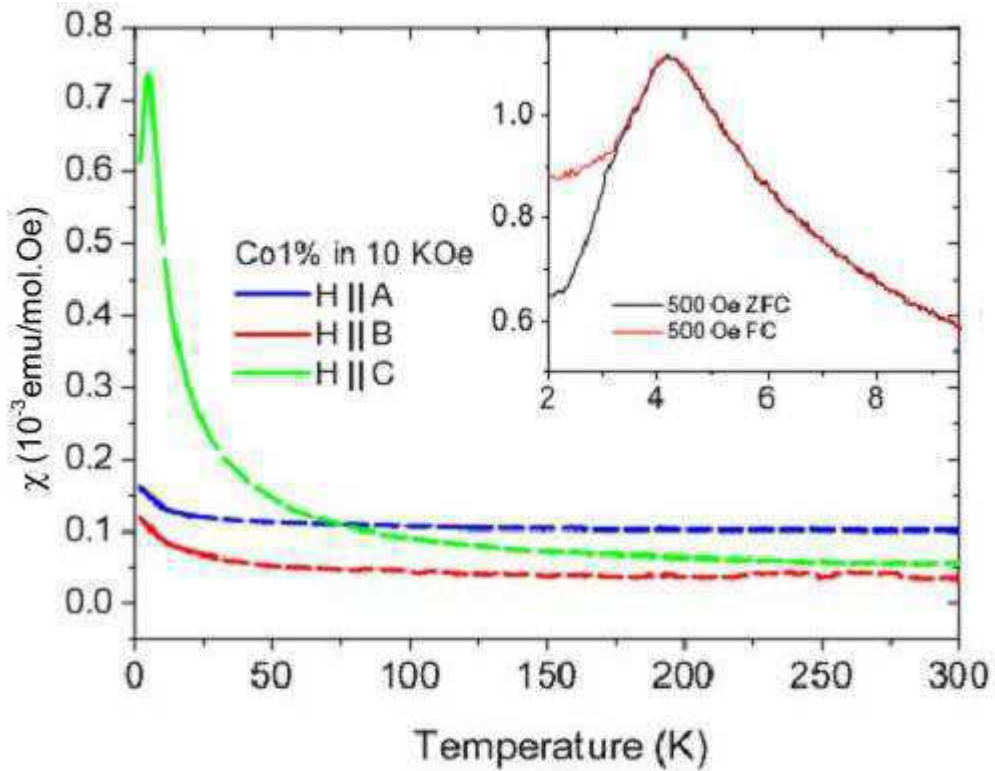


Figure 4.1: Magnetic susceptibility data of $\text{Sr}_{0.99}\text{Co}_{0.01}\text{CuO}_2$ along the three crystallographic directions. Inset: ZFC and FC data of susceptibility below T_p

4.1.1 Effect of Magnetic Impurity

Susceptibility measurements performed along the three crystallographic directions for $\text{Sr}_{0.99}\text{Co}_{0.01}\text{CuO}_2$ are shown in Figure 4.1

No fit for the magnetic susceptibility using Eq.4.1 is possible for the obtained data. The susceptibility measured along the chain direction shows a strong anisotropic increase below 150K with an ordering transition peak around 5K . Moreover, around 2K - 2.5K below the main transition peak (T_p), Zero Field Cooled (ZFC) and Field Cooled (FC) measurements of susceptibility at 500Oe clearly show a splitting which is a clear signature of spin glass/spin freezing behaviour. The magnetization measurements at 2K also reveal a small M-H hysteresis loop which supports the suggestion of glassy behaviour of spins at these temperatures.

The peak in susceptibility exists for all the doping concentrations of Co (0.25% , 0.5% , 1%), however the temperature (T_p) at which the transition takes place is found to scale almost linearly with the concentration of Co as shown in Figure 4.3. This can be seen as strong evidence that the transition peak is not

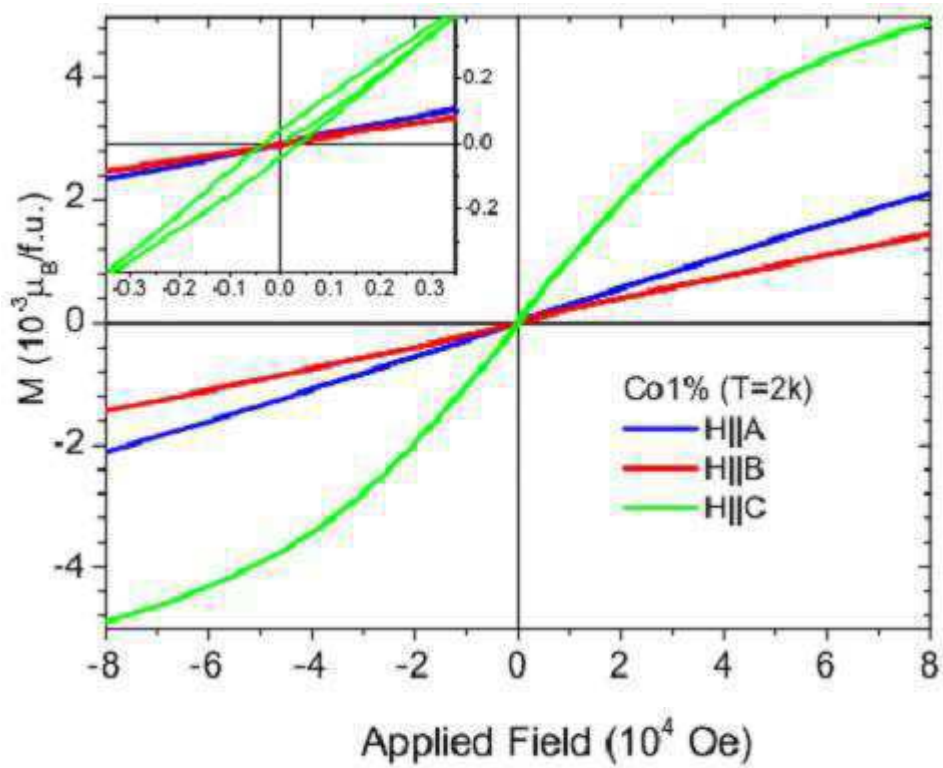


Figure 4.2: M vs H curve for $\text{Sr}_{0.99}\text{Co}_{0.01}\text{CuO}_2$ measured at 2K. Inset: Magnified M-H data for very small applied fields reveals a hysteresis loop

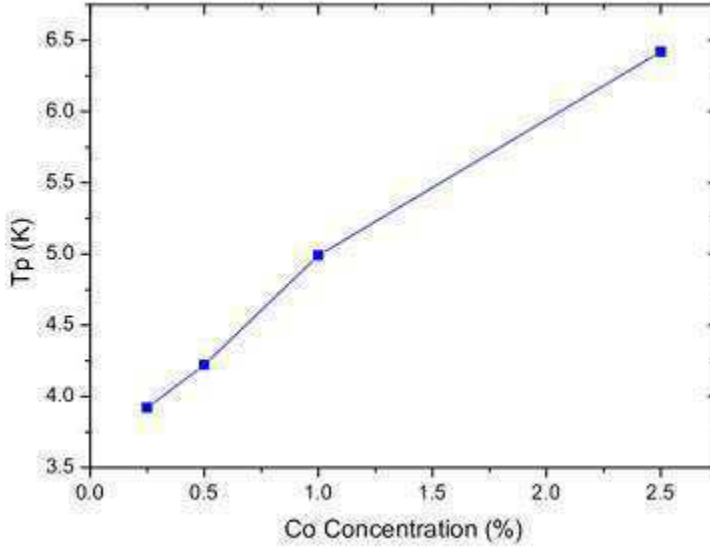


Figure 4.3: The dependence of T_p on concentration of Co doping

due to the establishment of long range order (LRO) as observed in Sr_2CuO_3 . This is because Neel-like LRO is a “disorder to order” bulk transition which involves spontaneous 3D ordering of the entire magnetic lattice. If we assume the establishment of LRO at T_p for 0.25% Co, then T_p for 0.5% Co and 1% Co should not show any appreciable variation with the the concentration of the doped impurities. However, we have evidence to the contrary.

Additionally, the presence of another transition below T_p indicates that the transition at T_p is not due to Neél ordering (which is a “disorder to order” transition). The fact that the system reorders below T_p clearly suggests that the ordering is not Neél-like. Instead, the strong dependence of T_p on the concentration of the dopant suggests some kind of effective interaction between the impurity moments which depends inversely on the average separation between the impurity moments. Higher doping concentrations imply lesser average separation between the moments which would lead to an increase in the strength of the effective interaction between the moments, thus explaining the shift of T_p to higher temperatures.

It is clear that Co drastically alters the magnetic ground state of the system. Co is known to show anisotropic magnetic behaviour due to an unquenched orbital contribution. Assuming that the Co^{2+} ions are in their high-spin (HS) state, then in the square planar coordination the splitting of the d -orbitals of Co is as shown in Figure 4.4(d)

The e_g orbitals (d_{z^2} and $d_{x^2-y^2}$) have completely quenched orbital angular momentum. The spin-orbit coupling is irrelevant for these states. On the other hand, an incompletely filled t_{2g} shell can have a pseudo orbital moment of

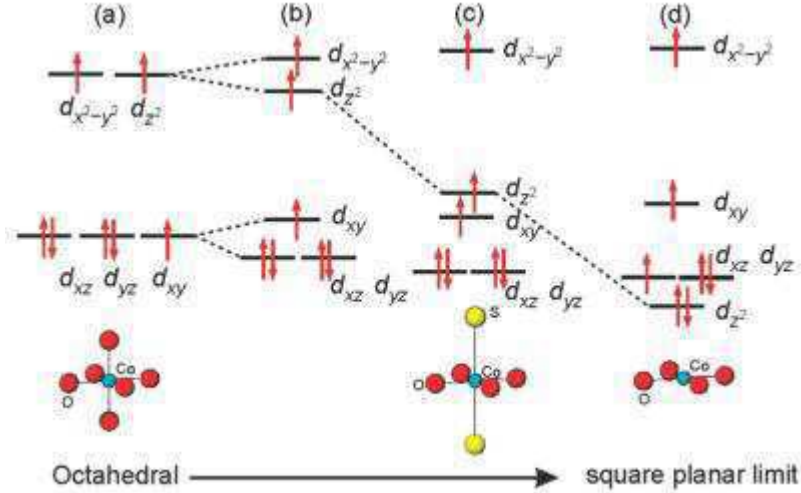


Figure 4.4: The d orbital splitting for high-spin Co²⁺ with O²⁻ ranging from purely octahedral (a) to purely square planar (d) via a slightly tetragonally elongated octahedron (b) and the highly tetragonally elongated arrangement (c) [38].

$\tilde{L} = 1$ [37]. This is due to the fact that eventhough the basis wave functions d_{xy} , d_{yz} and d_{xz} are *real*, their linear combinations are in general *complex*. Therefore, we can have new wavefunctions with their orbital moment quantized along the x , y and z axis respectively as,

$$d_{\pm 1}^x = \frac{1}{\sqrt{2}}(\pm d_{xy} + i d_{xz}) \quad (4.2)$$

$$d_{\pm 1}^y = \frac{1}{\sqrt{2}}(\pm d_{yz} + i d_{xy}) \quad (4.3)$$

$$d_{\pm 1}^z = \frac{1}{\sqrt{2}}(\pm d_{xz} + i d_{yz}) \quad (4.4)$$

In the case of a partially filled t_{2g} shell with a large crystal field splitting between the t_{2g} and e_g levels in an octahedral environment, the moment is *isotropic*. The isotropy arises due to the fact that in an incompletely filled t_{2g} shell all the linear superpositions listed above exist and are degenerate. The t_{2g} electrons have even been compared to p electrons because of this isotropy [39].

The orbital moment can show anisotropic behaviour if there is a crystal field of a lower symmetry which will lead to a further splitting of the t_{2g} and e_g levels. A tetragonal crystal field (relevant to Co doped in SrCuO₂) splits the e_g states into non-degenerate a_{1g} and b_{1g} levels, while the t_{2g} level splits into a non-degenerate b_{2g} (d_{xy}) state and a two-fold degenerate e'_g (d_{xz} and d_{yz}) level.

If we now consider the case of Co^{2+} , a low spin (LS) scenario would mean that the b_{2g} level and the e'_g level are completely occupied. Therefore there is only one hole which resides in one of the split e_g state (either a_{1g} or b_{1g}). Thus, the LS configuration of Co^{2+} cannot be expected to show anisotropic behaviour of the magnetic moment *in a tetragonal crystal environment*, as there is no orbital contribution to the total angular momentum. On the other hand, the high spin (HS) configuration for Co would imply two holes in the e_g levels and a single hole in one of the t_{2g} levels. The single hole can occupy either the non-degenerate b_{2g} state (d_{xy}) [corresponding to an elongation along the z -axis] or the two-fold degenerate e'_g state (d_{xz} and d_{yz}) [corresponding to a compression along the z -axis]. Let us consider each case in turn:

1. If the hole is present in the degenerate d_{xz} and d_{yz} orbitals, it will essentially occupy a linear combination of the d_{xz} and d_{yz} orbitals, which is precisely what Eq. 4.4 represents. The spin-orbit interaction will lead to a state with the orbital moment of $1\mu_B$ directed along the z -direction. The spin moment (and hence the magnetic moment) will also be constrained to point along this direction due to the spin-orbit coupling.
2. If the hole is present in the non-degenerate d_{xy} orbital, then no linear combinations like the ones in Eqns. 4.2, 4.3 and 4.4 are possible. The orbital moment in this case would be completely quenched, as a consequence the magnetic moment would be expected to show isotropic behaviour in conformity with the isotropic nature of the spin moments. However, there is a caveat here: If the magnitude of the spin-orbit coupling is the same or greater than the splitting between the b_{2g} state and the e'_g state, then it can lead to a mixing between the states and result in a net orbital moment contribution.

It can be inferred from Figure 4.4 that in the square planar limit (*which is of relevance for our system*), there will be a large orbital contribution directed along the z -direction. This is due to the presence of a single hole in the e'_g level which occupies a linear superposition of the two orbitals d_{xz} and d_{yz} (as given by Eq. 4.4) and consequently leads to an orbital contribution along the z -direction. However, our susceptibility measurements reveal a huge anisotropy along the crystallographic c -direction which suggests that the orbital contribution lies along this axis. This suggests an even lower symmetry in the local environment of Co^{2+} which further splits up the degenerate e'_g levels. It must be pointed out here that while Figure 4.4d illustrates the splitting for the HS state of Co, even for Co in LS state there will be a finite orbital contribution which would lead to an anisotropic behaviour of the spin of Co. Another point to remember is that in order for the orbital contribution to be present along the c -direction the magnitude of the spin-orbit interaction has to match the splitting between the d_{xy} and d_{xz} (or d_{yz}) orbitals.

An important piece of information that we can get out of the discussion above is that Co ions lead to a local distortion in the lattice which should lead to:

- Modulation of the exchange integral, J , in the neighbourhood of the Co ions.
- Local distortion of the lattice which will act as an effective scatterer for phonons.

Both of these are expected to play an important role in determining the dynamical behaviour of the elementary excitations of the system which can be verified from transport measurements. This is our topic for discussion in the next section.

4.2 Thermal Transport

4.2.1 Effect of Magnetic Impurity (Co)

Evidence for ballistic heat transport in SrCuO₂ was first reported by Hlubek et al [40]. The dramatic increase in the magnetic contribution to thermal conductivity along the spin chains with an increase in the purity of the precursors (particularly CuO) provided clear proof of ballistic heat transport in SrCuO₂. The aim of the present study was to probe the effect of doping of magnetic and non-magnetic impurities in the spin chains. Unfortunately, no data for the non-magnetic impurities could be obtained. In this section, we focus on the magnetic dopant (Co²⁺). Irrespective of whether the Co ions are in the high spin state (S=3/2) or the low spin state (S=1/2) the spins are half-integer multiples. This is in contrast to the case of Ni which has an integer spin (S=1), which was investigated as a magnetic dopant in [16].

4.2.1.1 Co = 0.25%

The thermal conductivity measured along the crystallographic c and a directions are shown in Fig. 4.5 . The maximum value of the thermal conductivity measured along c , κ_c is ≈ 560 W/K/m at a temperature 18.5K which is about 0.6 times less than for pure SrCuO₂ (see Figure 4.6). A comparison with Ni reveals that the thermal conductivity κ_c of the Ni sample is higher than Co for the same concentration of doping around the region of the peak (Figure 4.6), however κ_c of Co clearly exceeds κ_c of Ni above 50K. A comparison of κ_a shows that there is an anomalous increase in the phononic conductivity along the a -direction for Ni, which also explains the increase of the peak along the c -direction. A comparison at high temperatures of the thermal conductivity, κ_c , also reveals that κ_c of Co exceeds κ_c of Ni upto room temperature. The contribution due to magnetic excitations was obtained by subtracting the phononic contribution from κ_c . Thus,

$$\kappa_{mag} = \kappa_c - \kappa_a \quad (4.5)$$

According to the discussion in Section 3.2.3, due to large errors expected at low temperatures, only the data above 50 K is taken into consideration. κ_{mag}

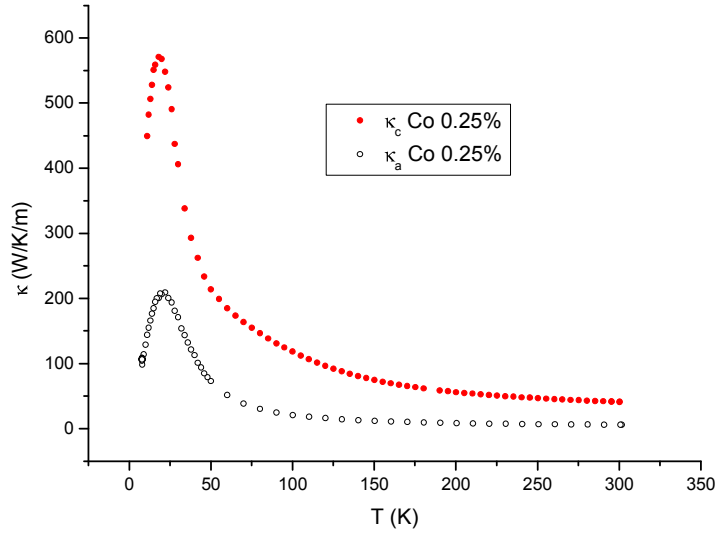


Figure 4.5: κ_c (red circles) and κ_a (black open circles) of $\text{SrCu}_{0.9975}\text{Co}_{0.0025}\text{O}_2$

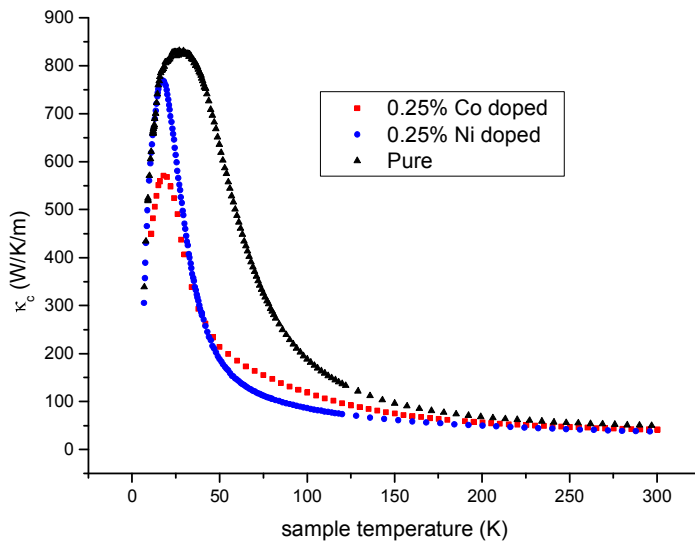


Figure 4.6: κ_c of 0.25% Co doped (red squares), 0.25% Ni doped (blue circles) and pure SrCuO_2 (black triangles)

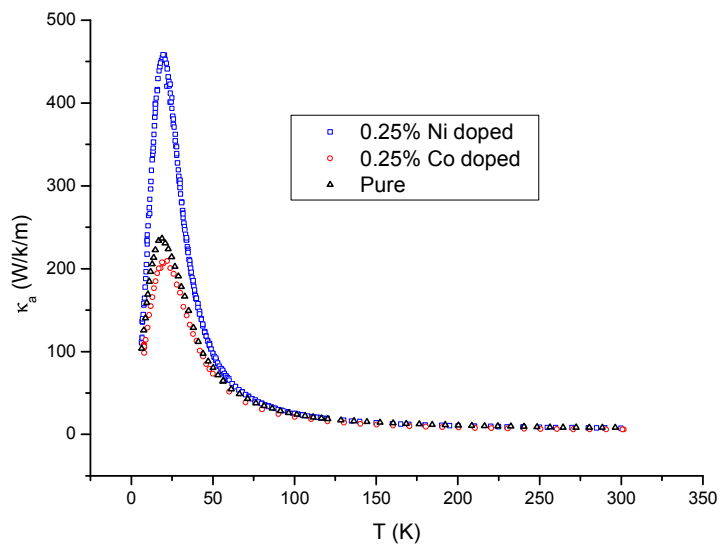


Figure 4.7: κ_a of 0.25% Co doped (red open circles), 0.25% Ni doped (blue open squares) and pure SrCuO_2 (black triangles).

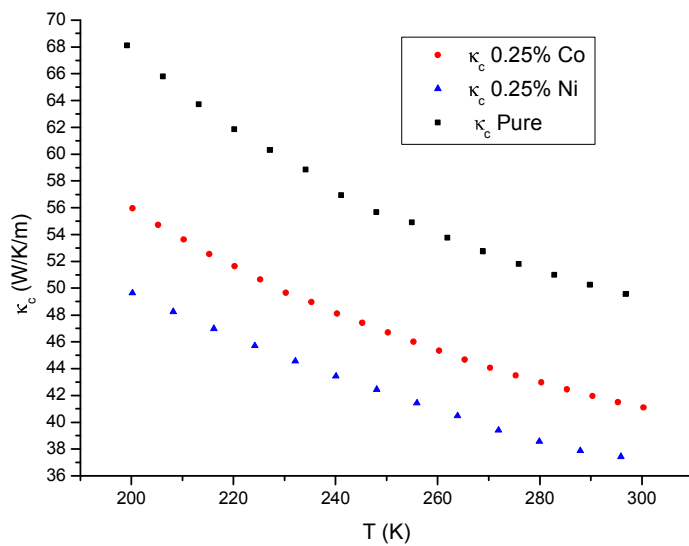


Figure 4.8: High Temperature Comparison of κ_c of 0.25% Co (red circle), 0.25% Ni (blue triangle) and Pure SrCuO₂ (black squares)

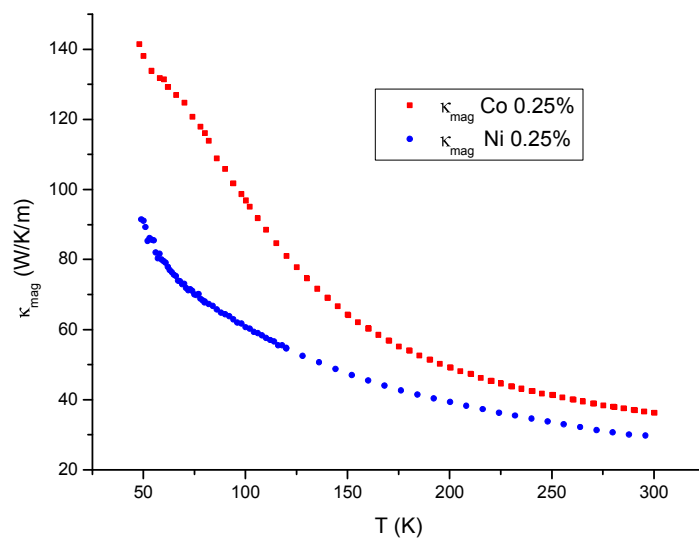


Figure 4.9: Comparison of κ_{mag} of 0.25% Co doped (red squares) and 0.25% Ni doped (blue circles) SrCuO₂

	$l_0(\mu\text{m})$	T_u^* in K	A_s in $10^{-6}\text{m}^{-1}\text{K}^{-1}$
2N	0.3	219	81.6
4N	1.48	209	61.2
0.25% Co	0.22	202.5	66.8
1% Co	0.15	147	56.9

Table 4.1: Fit Parameters for the Magnetic Mean Free Path using Eq. 1.47

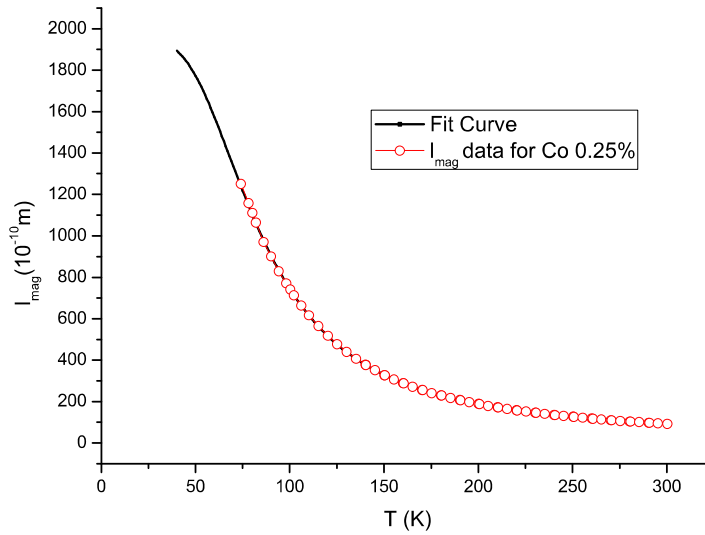


Figure 4.10: l_{mag} obtained for 0.25% Co doped SrCuO_2 (red open circles) along with the fitted curve (solid black line) using Eq. 1.47

obtained using Eq. 4.5 for both 0.25% Co and 0.25% Ni are shown in Figure 4.9.

κ_{mag} was analyzed quantitatively by extracting the spinon mean free path l_{mag} using the Drude weight D_{th} approach. The extracted l_{mag} obtained in the temperature range of 50K - 300K is plotted in Figure 4.10. The parameters obtained for the fit using Eq. 1.47 are summarized in Table 4.1. A comparison of the value of l_0 which is the mean free path of spinons between defects shows that l_0 is about 0.66 times the value l_0 for an undoped sample with 2N purity (data for 2N and 4N purity samples was taken for comparison from [16]), while it is 0.15 times the value of l_0 for an undoped sample of 4N purity. This indicates that Co is not acting simply as a point defect in the chains but is leading to the confinement of the spinons, which may explain the reduced magnitude of l_0 for the Co doped sample.

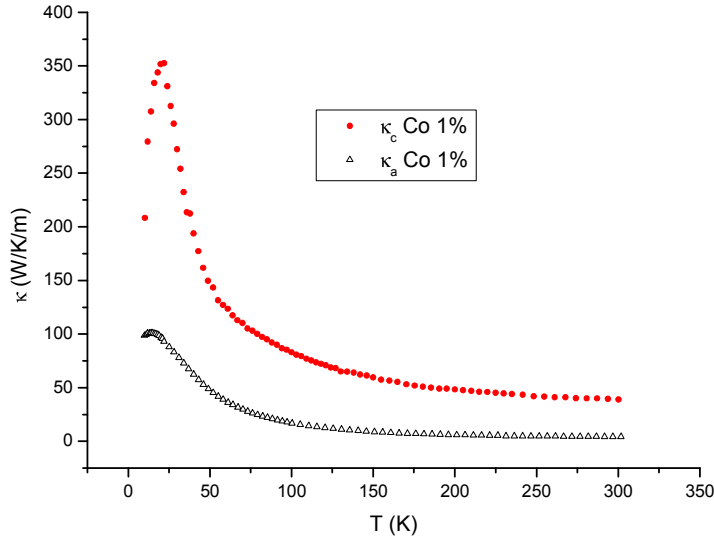


Figure 4.11: κ_c (red circles) and κ_a (black open circles) of $\text{SrCu}_{0.99}\text{Co}_{0.01}\text{O}_2$

4.2.1.2 Co = 1%

The thermal conductivity measured along the crystallographic c and a directions for 1% Co are shown in Figure 4.11. The maximum value of the thermal conductivity, κ_c , is suppressed further to ≈ 350 W/K/m at a temperature of ≈ 18.5 K. A comparison with Ni for the same doping concentration again reveals that the thermal conductivity κ_c of the Ni sample is higher than Co for the same concentration of doping around the region of the peak (Figure 4.12), however the enhancement in the peak in Ni doped sample is again understood to be due to phonons. κ_c of Co again exceeds that of Ni above 50 K and continues to be greater up to room temperature (see Figure 4.14). The contribution due to magnetic excitations was again obtained by subtracting the phononic contribution from κ_c . Thus, κ_{mag} obtained by using Eq. 4.5 for both 1% Co and 1% Ni are shown in Figure 4.15. The extracted l_{mag} obtained in the temperature range 50 K - 300 K is plotted in Figure 4.16. The parameters obtained for the fit using Eq. 1.47 are summarized in Table 4.1. A comparison of l_{mag} for both concentrations of Co is shown in Figure. 4.17

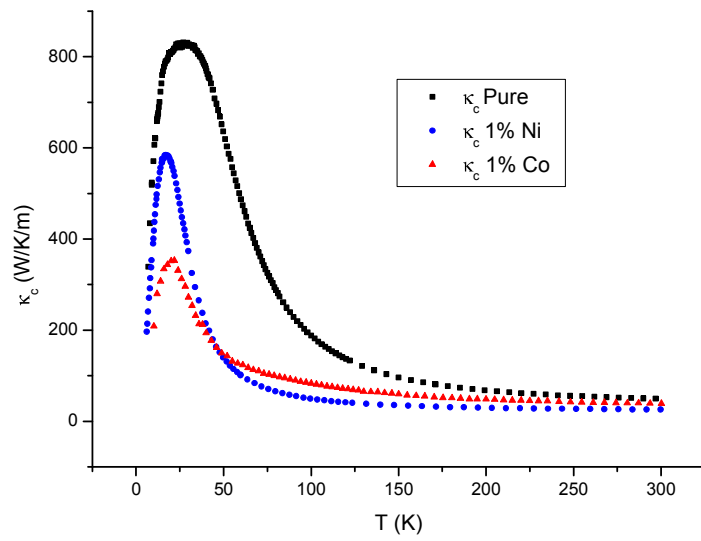


Figure 4.12: κ_c of 1% Co doped (red triangles), 1% Ni doped (blue circles) and pure SrCuO_2 (black squares)

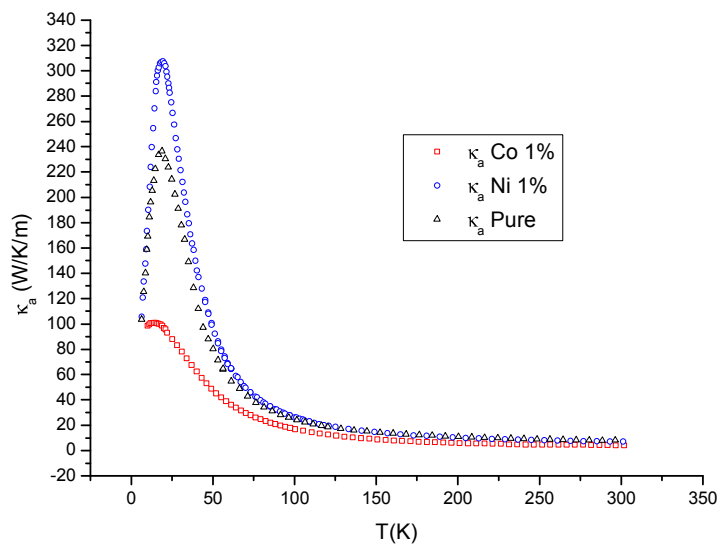


Figure 4.13: κ_a of 1% Co doped (red open circles), 1% Ni doped (blue open squares) and pure SrCuO₂ (black open triangles).

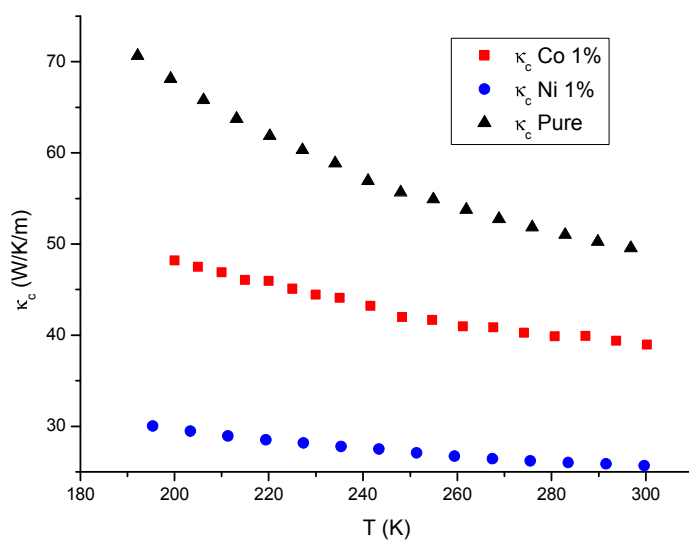


Figure 4.14: High Temperature Comparison of κ_c of 1% Co (red squares), 1% Ni (blue circles) and Pure SrCuO₂ (black triangles)

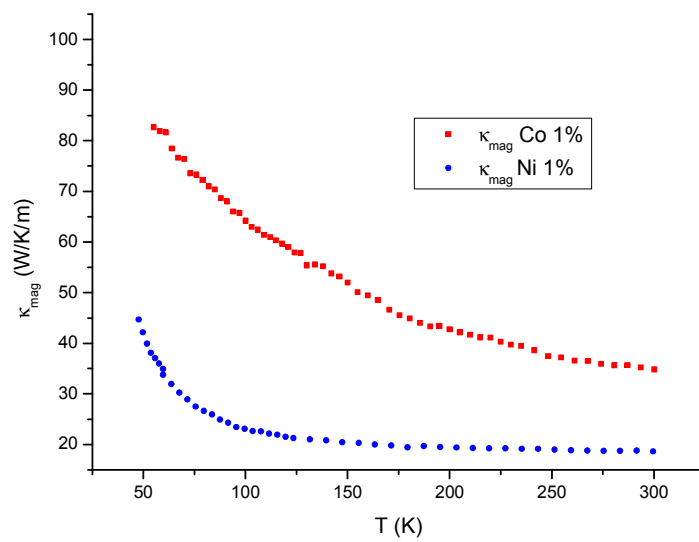


Figure 4.15: Comparison of κ_{mag} of 1% Co doped (red squares) and 1% Ni doped (blue circles) SrCuO₂

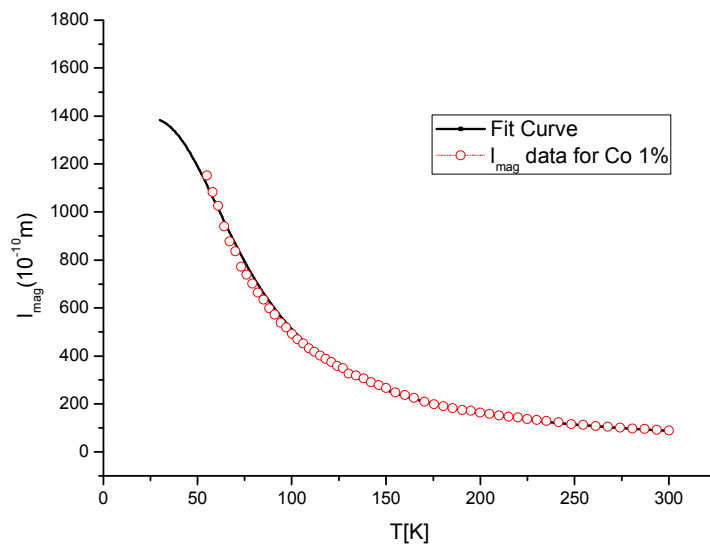


Figure 4.16: l_{mag} obtained for 1% Co doped SrCuO_2 (red open circles) along with the fitted curve (solid black line) using Eq. 1.47

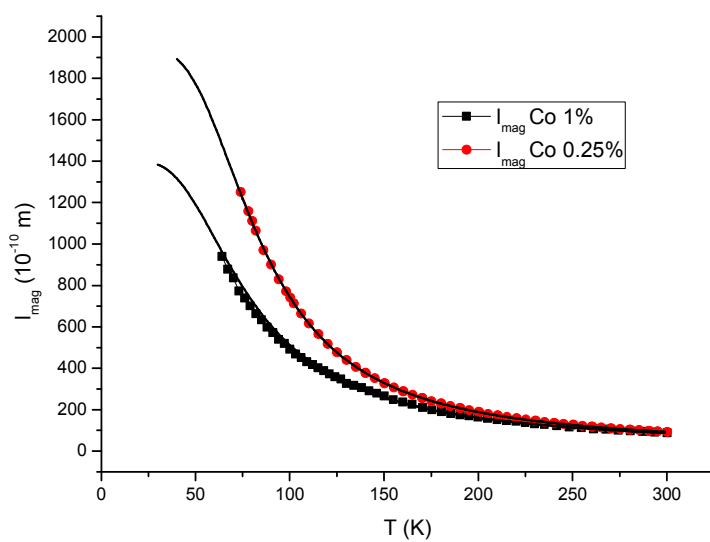


Figure 4.17: Comparison of l_{mag} for 0.25% Co doped and 1% Co doped SrCuO_2 along with fitted curves (solid black lines) using Eq. 1.47

Part V

Summary

Chapter 5

Attempt towards a coherent picture

It is quite amazing to note the drastically different behaviours that the two different magnetic impurities induce in the quasi-1D quantum magnets. Ni which is an $S = 1$ impurity induces a spin gap [16]. We know that a spin gap appears in the following cases:

- Finite size of the spin chain
- Anisotropy in the spin chain
- Spin-Integer chains (Haldane Gap)

In principle, it should be possible to identify one of the cases listed above as the causative agent when a spin gap appears in any system. However, this is difficult due to the complex inter-relation of the various couplings present in the lattice (this has already been discussed for the frustrated coupled ladder system in the **Introduction**).

The thermal transport measurements on Ni doped samples of SrCuO_2 by Nikolai [16] indicate the absence of low-energy excitations along the spin chain, this together with the observation of a spin gap implies an exponential decay of the correlation function. This is an extraordinary result as this behaviour is the signature of antiferromagnetic chains with integer spins. According to Haldane [45, 46], $S = 1$ antiferromagnetic Heisenberg spin chains are disordered at $0K$, with a correlation function which decreases exponentially at large distance as,

$$\langle \mathbf{S}_i \cdot \mathbf{S}_j \rangle \propto (-1)^{(i-j)} e^{-(|\mathbf{R}_i - \mathbf{R}_j|/\zeta)} \quad (5.1)$$

where ζ is the correlation length along the spin chain.

It does not appear to be reasonable to expect the entire chain to behave like a chain comprising of integer spins, nevertheless only by the determination of the correlation length in the spin chains by a magnetic probe can this mystery

be cleared. Just to emphasize the dramatic effect of Ni spins on the behaviour of the spin chain, note that Ni does not exhibit any on-site anisotropy, thus opening of a spin gap opening due to anisotropy can be ruled out. We are therefore left with either the contribution of the finite size or the spin integer case. Thermal conductivity measurements for the case of Mg ($S = 0$) doping [16], which breaks the chain into finite segments does not show any significant suppression of the magnetic contribution to conductivity along the spin chains. All of the measurements therefore appear to point towards a radical change to spin integer behaviour at low temperatures for Ni doping.

Continuing with the discussion for the case of Ni doped samples, an anomalous increase in the phonon contribution along the directions perpendicular (as well as parallel) to the chain direction was observed. In [16] the explanation given for such an increase in the phonon conductivity along the direction perpendicular to the chain is that the spinons at low temperatures which used to scatter some of these phonons in the pure compound are now absent in the Ni doped crystals, thus in the absence of the spinons which acted as scatterers, the phonon conductivity is enhanced. In the following text, an attempt is made to elaborate a little more on this idea.

To begin with, it must be emphasized that for the low-energy excitations to be established in the chain, the magnitude of the coupling J between the nearest neighbours comprising a 1D spin chain should be uniform. Any modulation in J results in the confinement of the spinons (as seen for Ca doping of SrCuO₂ [16]). From the information obtained from measurements done on the Ni doped samples, it appears that in pure SrCuO₂ there is a resistance to change of the exchange coupling J . Any phonon mode which would result in the modification/modulation of the exchange integral gets suppressed. A more useful way to model such a behaviour where we take recognition of the soliton-like behaviour of the spinons is to assume that the spinons act as effective point scatterer/defects. Thus, according to this model some of the phonon modes perceive these fast moving spinons as defects. A merit of this scheme is that since the spinons are always created in pairs, the one which propagates away from the heat bath towards the heat sink is almost never scattered due to the phonons since the phonons are comparatively very slow moving excitations. These spinons are therefore unaffected and contribute to the conduction of heat, while the other may get scattered due to a phonon. The modelling of spinons as dynamic point defects is also consistent with the experimental observation that the enhancement of the phonon contribution for Ni doping occurs most prominently in the regime (region around the peak) where defect scattering is the dominant scattering mechanism.

For Co doped samples, which induces an anisotropy in the chains, there must be a finite gap in the spin excitation as well. However, the thermal conductivity measurements on the two concentrations of Co indicate that the size of this gap is not comparable to the gap induced by Ni. The reduction in the thermal conductivity therefore appears to arise from modulation of the exchange integral in the spin chain which leads to a confinement of the spinons. The fact that the phonon contribution also decreases substantially, indicates a local distur-

tion in the lattice due to the Co ions which further supports the assertion of the modulation of J . The susceptibility measurements for all the doping concentrations of Co (0.25%, 0.5%, 1%) reveal that the temperature (T_p) at which the transition takes place, scales almost linearly with the concentration of Co. This indicates that the transition peak is not due to the establishment of Neél-like long-range-order (LRO) as observed in Sr_2CuO_3 . This is because Neél-like LRO is a “disorder to order” bulk transition which involves spontaneous 3D ordering of the entire magnetic lattice. If Neél order is established at T_p for 0.25% Co, then T_p should not show an appreciable change for 0.5% Co and 1% Co.

The presence of another transition below T_p further supports the assertion that the transition at T_p is not due to Neél ordering (which is a “disorder to order” transition). The fact that the system reorders below T_p clearly suggests that the ordering is not Neél-like. Instead, the strong dependence of T_p on the concentration of the dopant suggests some kind of effective interaction between the impurity moments which depends inversely on the average separation between the impurity moments. Higher doping concentrations imply lesser average separation between the impurity moments. Consequently, there is an increase in the strength of the effective interaction between the moments with increased doping concentration, which would explain the shift of T_p to higher temperatures.

Additionally, Zero Field Cooled (ZFC) and Field Cooled (FC) measurements of susceptibility around 2K-2.5K below the main transition peak (T_p), at 500 Oe clearly show a splitting which is a clear signature of spin glass/spin freezing behaviour[47].

Further experimental studies which probe the local level behaviour of the spins in the Co doped systems are expected to provide further insight into the physics of this system.

Bibliography

- [1] Hulthén, L.: Ark. Mater. Astron. Fys. A **26**, 11-116 (1938)
- [2] H-J Mikeska, A. K. Kolezhuk, Lec. Notes Phys. **646**, 1-83(2004)
- [3] Heisenberg W., Z. Phys. **49**, 619 (1928)
- [4] Bethe, H. A.: Z. Phys. **71**, 205-226 (1931)
- [5] E. Ising: Z. Physik **31**, 253 (1925)
- [6] Onsager, L., Phys. Rev., **65**, 117 (1944)
- [7] Anderson, P. W.: Phys. Rev. **86**, 694 (1952)
- [8] Oguchi, T.: Phys. Rev. **117**, 117 (1960)
- [9] Parkinson, J. B., Farnell, D. J. J.: An Introduction to Quantum Spin Systems, Lect. Notes Phys. 816 (Springer, Berlin Heidelberg 2010)
- [10] Mermin N. D.,Wagner H.: Phys. Rev. Lett. **17**, 1133 (1966)
- [11] S. Eggert, I. Affleck, and M. Takahashi, Phys. Rev. Lett. **73**, 332 (1994)
- [12] N. Motoyama, H. Eisaki, S. Uchida: Phys. Rev. Lett. **76**, 3212 (1996)
- [13] D. C. Johnston, R. K. Kremer, M. Troyer *et al*, Phys. Rev. B. **61**, 9558 (2000)
- [14] J. Cloizeaux, J. J. Pearson, Phys. Rev. **128**, 2131 (1962)
- [15] Patrick Ribeiro, PhD Thesis, Technische Universität (TU) and Leibniz Institute for Solid State Research (IFW) , Dresden (2007)
- [16] Nikolai Hlubek, PhD Thesis, Technische Universität (TU) and Leibniz Institute for Solid State Research (IFW) , Dresden (2010)
- [17] C. Hess, Eur. Phys. J. Special Topics **151**, 73 (2007)
- [18] Callaway, Quantum Theory of the Solid State, Academic Press, London (1991)

- [19] X. Zotos, F. Naef, and P. Prelovsek, Phys. Rev. B **55**, 11029 (1997)
- [20] T. Niemeijer and H. A. W. van Vianen, Phys. Lett. A **34**, 401 (1971)
- [21] A. Klümper and K. Sakai, J. Phys. A: Math. Gen. **35**, 2173 (2002).
- [22] A. Matthiessen, Phil. Trans. R. Soc. London **148**, 383 (1858), ISSN 02610523
- [23] A. Matthiessen and C. Vogt, Phil. Trans. R. Soc. London **154**, 167 (1864), ISSN 02610523
- [24] G. A. Slack and S. Galginitis, Phys. Rev. **133**, A253 (1964).
- [25] C. J. Glassbrenner and G. A. Slack, Phys. Rev. **134**, A1058 (1964)
- [26] M.-R. Li and E. Orignac, Europhys. Lett. **60**, 432 (2002)
- [27] A. V. Rozhkov and A. L. Chernyshev, Phys. Rev. Lett. **94**, 087201 (2005)
- [28] A. L. Chernyshev and A. V. Rozhkov, Phys. Rev. B **72**, 104423 (2005)
- [29] S. Gangadharaiah, A. L. Chernyshev, and W. Brenig, arXiv:1006.3949v1 (2010).
- [30] E. Shimshoni, N. Andrei, and A. Rosch, Phys. Rev. B **68**, 104401 (2003)
- [31] B. Normand, K. Penc, M. Albrecht, F. Mila, Phys. Rev. B **56**, R5736 (1997)
- [32] W. Pfann, Journal of Metals **194**, 747 (1952).
- [33] J. Shah, Crystal Growth, Chapter 4, pages 113–116, Pergamon Press, 1975
- [34] B. R. Pamplin, Crystal Growth, Pergamon Press Oxford, 1975
- [35] W. Wong-Ng, L. P. Cook and W. Greenwood, Physica C: Superconductivity **299**, 9 (1998)
- [36] J. Sirker, N. Laflorencie, S. Fujimoto, S. Eggert, I. Affleck, Phys. Rev. Lett. **98**, 137205 (2007)
- [37] Hollman *et al*, New J. Phys. **10**, 023018 (2008)
- [38] C. F. Smura, D. R. Parker, M. Zbiri, M. R. Johnson, Z. A. Gál, S. J. Clarke, J. Am. Chem. Soc., **133**, 2691 – 2705 (2011)
- [39] H. Kamimura, J. Phys. Soc. Japan **11**, 1171 (1956)
- [40] N. Hlubek, P. Ribeiro, R. Saint. Martin, A. Revcolevschi, G. Roth, G. Behr, B. Buechner, C. Hess, Phys. Rev. B **81**, 020405 (2010)
- [41] J. Villain, Physica B **79** (1975)
- [42] Ishimura. H. Shiba: Progr. Theor. Phys. **63**. 743 (1980)

- [43] S. R. White and I. Affleck, Phys. Rev. B **54**, 9862 (1996)
- [44] Goran Jan Nilsen, PhD Thesis, University of Edinburgh (2010)
- [45] Haldane F D M, Phys. Lett. A **93**, 464 (1983)
- [46] Haldane F D M, Phys. Rev. Lett. **50**, 1153 (1983)
- [47] J. A. Mydosh, Journal of Magnetism and Magnetic Materials **157/158**, 606-610 (1996)
- [48] J. B. Goodenough, J. Phys. Chem. Solids, **6**, 287-297 (1958)
- [49] J. Kanamori, J. Phys. Chem. Solids, **10**, 87-90 (1959)